Low Temperature Laboratory, Department of Applied Physics

Quantum noise correlations and amplifiers in mesoscopic systems

Pasi Lähteenmäki

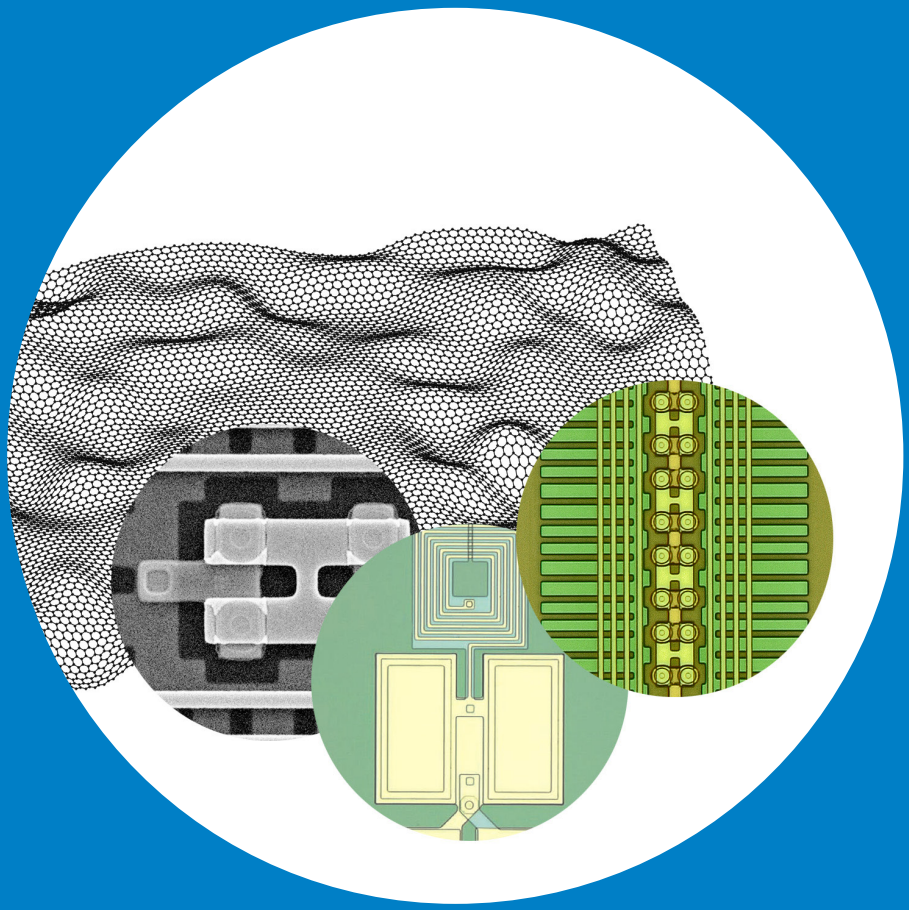

Aalto University

DOCTORAL DISSERTATIONS

Aalto University publication series
DOCTORAL DISSERTATIONS 13/2016

Quantum noise correlations and amplifiers in mesoscopic systems

Pasi Lähteenmäki

A doctoral dissertation completed for the degree of Doctor of Science (Technology) to be defended, with the permission of the Aalto University School of Science, at a public examination held at the lecture hall AS1 of TUAS on 25th January 2016 at 12:00.

Aalto University
School of Science
Low Temperature Laboratory, Department of Applied Physics
Nano

Supervising professor
Prof. Pertti Hakonen

Preliminary examiners
Dr. Frank Deppe, Walther-Meißner-Institut, Germany
Dr. Benjamin Huard, CNRS / Ecole Normale Supérieure, France

Opponent
Prof. Per Delsing, Chalmers University of Technology, Sweden

Aalto University publication series
DOCTORAL DISSERTATIONS 13/2016

ISBN 978-952-60-6627-1 (printed)
ISBN 978-952-60-6628-8 (pdf)
ISSN-L 1799-4934
ISSN 1799-4934 (printed)
ISSN 1799-4942 (pdf)
http://urn.fi/URN:ISBN:978-952-60-6628-8

Unigrafia Oy
Helsinki 2016

Finland

441 697
Printed matter

Aalto University

Abstract

Aalto University, P.O. Box 11000, FI-00076 Aalto www.aalto.fi

Author
Author

Name of the doctoral dissertation
Quantum noise correlations and amplifiers in mesoscopic systems

Publisher School of Science

Unit Department of Applied Physics

Series Aalto University publication series DOCTORAL DISSERTATIONS 13/2016

Field of research Experimental Mesoscopic Physics

Manuscript submitted 5 October 2015 **Date of the defence** 25 January 2016

Permission to publish granted (date) 17 December 2015 **Language** English

☐ **Monograph** ☒ **Article dissertation (summary + original articles)**

Abstract

This thesis work deals with a range of superconducting devices operated near the fundamental performance limits set by quantum mechanics along with the nature of quantum vacuum itself when perturbed by such devices. These devices are operated in a dilution refrigerator cooled down to sub-Kelvin temperatures. Low temperature is absolutely essential for quantum behavior of these devices and the minimal inherent noise contribution.

Biased, selectively damped superconducting tunnel junction, (also known as the Josephson junction) displaying negative differential resistance, was employed to construct a device capable of amplifying weak microwave signal reflections from it. This device can be operated near the intrinsic precision limits set by the Heisenberg's uncertainty principle.

Arrays of Superconducting Quantum Interference Devices (SQUIDs), operated below the critical current, can be used for metamaterial resonators whose resonant frequency can be quickly modulated by magnetic flux. These devices are operated as parametric amplifiers and they are capable of amplifying weak microwave signals near the quantum limit of noise. But more importantly, they are capable of perturbing the vacuum itself, which creates correlated photon pairs seeded by vacuum fluctuations. This effect is known as the dynamical Casimir effect (DCE) and is demonstrated in this thesis work by using power and correlation measurements at microwave frequencies. Furthermore, investigations on the DCE have been extended using a double modulation scheme yielding vacuum-induced coherence and tripartite correlations.

Nanocarbon devices have also been studied in this thesis, in particular a wideband low noise nanotube electrometer constructed from a nanotube with proximity induced superconductivity. This device has certain unique benefits when operated in a microwave environment which are discussed in the thesis. Another nanocarbon device, a double quantum dot constructed from graphene and superconducting leads has been used to demonstrate Cooper-pair splitting. This device operates as a tunable source of entangled electrons.

Keywords Superconductivity, Nanoelectronics, Parametric amplifier, Dynamical Casimir effect, Metamaterial, Josephson junction, SQUID, Quantum mechanics, Carbon nanotube, Graphene, Cooper-pair

ISBN (printed) 978-952-60-6627-1 **ISBN (pdf)** 978-952-60-6628-8

ISSN-L 1799-4934 **ISSN (printed)** 1799-4934 **ISSN (pdf)** 1799-4942

Location of publisher Helsinki **Location of printing** Helsinki **Year** 2016

Pages 184 **urn** http://urn.fi/URN:ISBN:978-952-60-6628-8

Preface

The research presented in this thesis has been carried out in the Nano Group of the Low Temperature Laboratory, Department of Applied Physics at Aalto University.

I would like to begin by expressing my sincere gratitude to Prof. Pertti Hakonen for his guidance throughout all these years. I consider myself privileged having had the opportunity and freedom to work with him and this distinguished group and laboratory in general.

I acknowledge the tremendous support of my immediate professional collaborators, Sorin Paraoanu, Juha Hassel, Heikki Seppä, Dimitry Golubev, Andrey Timofeev, Visa Vesterinen, Aurélien Fay and Pasi Häkkinen. Numerous other professionals in and out of my host laboratory undoubtedly deserve my gratitude as well.

I wish to thank my fellow group members with whom I've worked closely, especially my colleague and friend Antti Puska, a humble man of many talents. I also acknowledge Xuefeng Song, Manohar Kumar, Zhenbing Tan, Daniel Cox, Antti Laitinen, Teemu Nieminen, Mika Oksanen and Matti Tomi. My former group members who've had a major influence on my life in the lab deserve a warm mention as well, Jayanta Sarkar, Dmitry Lyashenko and Lorenz Lechner.

Additionally I wish to thank Mika Sillanpää, Juha Pirkkalainen, Alexander Savin, Jari Penttilä, Mikko Kiviranta and Jaakko Sulkko for their the professional support. Many memorable dealings throughout the years with Maciej Weisner, Akira Hida, Jian Li, Khattiya Chalapat, Mathias Brandt, Raphael Chan, Sergey Danilin, Karthikeyan Sampath Kumar and Ville Kauppila should not be forgotten either.

Special acknowledgement to Joonas Varjonen, Tuomo Schwela, Tuukka Jousi, Juhani Kipinoinen, Ville Lilja, Suvi Kansikas and Annika Pöysä. Without all of you my life would have been much less diverse.

Reflecting a little, I must admit the surprising fact that these short years I've spent working for this laboratory have allowed me to grow both personally and professionally much more than the equivalent number of years before that. I'm very grateful for all the people who were involved in my life during this period. Being a bit of a lone wolf, I'm pleasantly surprised by the number of people who ended up having been acknowledged here. I'm eagerly looking forward to the future, but I can't entirely help myself feeling at least a little sad as this important era of my life is coming to an end.

Last, but definitely not least, I express my wholehearted gratitude to my wonderful parents, Ilmari and Tuula Lähteenmäki, without whom I could have never reached this far, you have been the best parents I could have ever hoped for and, should I have failed to express my true feelings on occasion, I hope you know that under the sometimes a bit cryptic exterior I have nothing but the warmest of feelings for the both of you.

Espoo, December 19, 2015,

Pasi Lähteenmäki

List of symbols and abbreviations

AC	Alternating current
AM	Amplitude modulation
CPS	Cooper pair splitter
DC	Direct current
EBL	Electron beam lithography
EC	Elastic cotunneling
FWHM	Full width at half maximum (the -3 dB bandwidth of a resonance)
HEMT	High-electron-mobility transistor
MWNT	Multi-wall nanotube
I, Q	In-phase and quadrature signal
IF	Intermediate frequency (of a frequency mixer)
IV	Current-voltage
JJ	Josephson junction
JPA	Josephson parametric amplifier
LNA	Low noise amplifier
LO	Local oscillator
RCSJ	Resistively and capacitively shunted junction (model)
RF	Radio frequency
RWA	Rotating-wave approximation
SEM	Scanning electron microscope
SET	Single electron transistor
SMA	Subminiature version A, a microwave connector
SIS	Superconductor-insulator-superconductor junction
S/N, SNR	Amplitude signal-to-noise ratio
SQUID	Superconducting quantum interference device
QD	Quantum dot
C	Capacitor or capacitance
C_G	Gate capacitance
C_J	Capacitance of a Josephson junction

e	Electron change, $e \approx 1.6022 \times 10^{-19} C$
E_J	Josephson energy
f	Frequency (Hz)
G	Power gain
h	Planck constant, $h \approx 6.62608 \times 10^{-34} Js$
$\hbar$	$h/2\pi \approx 1.0546 \times 10^{-34} Js$
i	Imaginary unit
I	Electric current (A)
I_b	Bias current (A)
I_C	Critical current (A)
k_B	Boltzmann constant, $k_B \approx 1.3807 \times 10^{-23} J/K$
L_J	Josephson inductance
R	Resistance (Ω)
R_d	Differential resistance (Ω)
S	Power spectral density of noise (typically in Kelvin)
S_{ku}	Scattering parameters
T	Temperature (K)
V	Voltage (V)
V_b	Bias voltage (V)
Z	Impedance (Ω)
Z_0	Standard transmission line impedance, $Z_0 = 50\Omega$
Γ	Voltage reflection coefficient
Δ	Superconducting energy gap
Δ_p	Frequency $\omega_p/2 - \omega_{\text{res}}$ corresponding to half of pump p
ω_p	Frequency of the pump p
ω_{res}	Resonant frequency of the cavity
κ	Total decay rate of a resonator
κ_i, κ_e	Internal and external decay rate of a resonator
Φ	Magnetic flux
Φ_0	Magnetic flux quantum, $\Phi_0 = h/2e \approx 2.0678 \times 10^{-15}\ Wb$
ω	Angular frequency (rad/s)
ω_J	Josephson junction plasma frequency
χ	Electrical susceptibility
$\langle\rangle$	Inner product or mean
$[]$	Commutator
$\{\}$	Anti-commutator
$\dagger$	Hermitian conjugate
*	Complex conjugate

Contents

List of Publications

This thesis consists of an overview and of the following publications which are referred to in the text by their Roman numerals.

I Pasi Lähteenmäki, Visa Vesterinen, Juha Hassel, Heikki Seppä, & Pertti Hakonen. Josephson junction microwave amplifier in self-organized noise compression mode. *Sci. Rep.*, 2, 276, February 2012.

II Pasi Lähteenmäki, G. S. Paraoanu, Juha Hassel, and Pertti J. Hakonen. Dynamical Casimir effect in a Josephson metamaterial. *Proc. Natl. Acad. Sci. U.S.A.*, 110, 4234-4238, March 2013.

III Z. B. Tan, D. Cox, T. Nieminen, P. Lähteenmäki, D. Golubev, G. B. Lesovik, and P. J. Hakonen. Cooper Pair Splitting by Means of Graphene Quantum Dots. *Phys. Rev. Lett.*, 114, 096602, March 2015.

IV Pasi Häkkinen, Aurelien Fay, Golubev Dimitry, Pasi Lähteenmäki, and Pertti J. Hakonen. Wideband superconducting nanotube electrometer. *Appl. Phys. Lett.*, 107, 012601, July 2015.

V Pasi Lähteenmäki, G. S. Paraoanu, Juha Hassel, and Pertti. J. Hakonen. Coherence from vacuum fluctuations under double parametric pumping. *Submitted to Nat. Commun. (Preprint: arXiv, 1512.05561)*, 1,20, December 2015.

Author's Contribution

The main contribution of the author in this thesis is in the experimental techniques and results obtained from quantum nanosamples in a dilution refrigerator at mK temperatures. Strong emphasis is placed on microwave noise power and current-current correlation measurements with further weight on fundamental understanding of quantum noise within these systems. The author was the key experimentalist in realizing the results on novel Josephson junction based devices and actively assisted with the measurements of nanocarbon samples.

Publication I: "Josephson junction microwave amplifier in self-organized noise compression mode"

The author designed the measurement setup, performed the experiments, collaborated in planning and design of the sample with Visa Vesterinen, Juha Hassel, Heikki Seppä and Pertti Hakonen. The author wrote the first version of the manuscript together with Visa Vesterinen.

Publication II: "Dynamical Casimir effect in a Josephson metamaterial"

The author took part in the planning of the work, built the measurement setup, performed the experiments and wrote the first version of the manuscript. The sample was designed by the author in collaboration with Juha Hassel. The author did circuit simulations for theoretical analysis of the data. Theoretical support was provided by G. Sorin Paraoanu. The paper was finished in collaboration with all of the authors.

Publication III: "Cooper Pair Splitting by Means of Graphene Quantum Dots"

The author took part in planning of the experimental setup and was involved in the transport experiments. The paper was written in collaboration with all the authors; the principal author was Zhenbing Tan.

Publication IV: "Wideband superconducting nanotube electrometer"

The author performed the measurements in collaboration with the principal author Pasi Häkkinen and assisted with the interpretation of the measurement data as well as writing of the paper.

Publication V: "Coherence from vacuum fluctuations under double parametric pumping"

This work extends the concepts investigated in Publication II. The author built the measurement setup, performed the experiments, analyzed the results and wrote the first version of the manuscript. The sample was designed by the author in collaboration with Juha Hassel who provided the sample. The author did all the simulations while theoretical support was provided by G. Sorin Paraoanu. The paper was finished in collaboration with all of the authors.

1. Introduction

The term "noise" is typically defined as something unwanted, some extra signal which interferes with the measurement of the actual signal, whether it be acoustic, electromagnetic or other power of interest. However, within the context of this thesis such a distinction is not the full story. For a device designed to observe phenomena, such as a photon counter or an electronic amplifier, the effect of noise is undoubtedly something which one hopes to eliminate. However, there is unavoidable quantum noise, a fundamental aspect of quantum mechanics. This noise can be regarded as being a consequence of Heisenberg's uncertainty principle, which states that there exists a minimum uncertainty between two conjugate quantum mechanical variables, such as position and momentum.

Within the context of this thesis, the relevant conjugate variables are the two orthogonal quadrature components of the electromagnetic field. RF-engineers know these as I and Q signals. No simple layman analogy exists, but perhaps the information (amplitude and phase) contained in these signals could be compared to the color of a photon and its arrival time. A standard form of the uncertainty principle exists between them as well.

The simplest consequence of this phenomenon is that the electromagnetic environment, whether it is the radiation in free space or the noise originating from a resistor in a closed system, cannot be "cooled" below a minimum equivalent temperature set by quantum mechanics. At 10 GHz, the equivalent power spectral density of this noise is about 0.24 Kelvin or -272.91 degrees of Celsius. This is extremely low value by everyday standards, but not particularly low for a dilution refrigerator. But, just like for two systems in thermal equilibrium, this state is special in such a way that no work can be extracted from it and, thus it cannot be detected in a direct manner, as it will not trigger any photon detector. One may also ar-

gue that no system can appear "colder" than that in regard to photons at that frequency. However, a system warmer than that can exist and then vacuum can absorb energy from this system. The vacuum here should not be confused with the cosmic microwave background which contains energy above that of a zero temperature emitter. Energy can be extracted from the CMB, and it can be measured directly.

In spite of not being directly detectable, vacuum fluctuations do have many observable consequences. One tangible consequence is that helium will not freeze at 0 K at low pressures. The kinetic energy guaranteed by the uncertainty principle in helium is so large relative to the strength of the bonds between helium atoms that the element will not solidify even at zero temperature.

Many of the experiments presented in this thesis manipulate the quantum vacuum in such a way that its signature will become encoded in the correlations and energy of the disturbances in the electromagnetic field introduced by an applied coherent source. These disturbances are directly seeded by the vacuum fluctuations. Strikingly, without the presence of these "actual qualities" there would be no signal whatsoever for us to observe in our experiments.

2. Fundamentals

This chapter will give a brief overview of the fundamental theoretical ideas behind the publications.

2.1 Josephson effect

The basic building block for active superconducting electronics at cryogenic temperatures is the superconducting tunnel junction, also known as the Josephson junction (JJ). The JJ is a weak link between superconductors [1,2]. This is typically realized as a thin insulating oxide between two metallic layers.

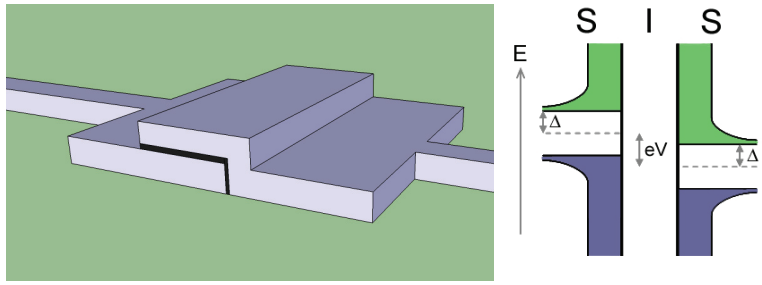

Figure 2.1. a) A JJ [3,4] formed by an insulator (black) between two layers of a superconducting metal. b) Energy diagram of a JJ. Energy on the vertical axis and density of states (DOS) on the horizontal. Cooper pairs exist at Fermi energy (dashed line). Bias voltage V shifts the Fermi energies of the superconductors relative to each other.

The JJ encompasses an inherent nonlinearity and it can by used as a threshold detector and as a source of both coherent and incoherent signals. The major advantage of a JJ is that it can, especially at low temperatures and frequencies, be considered as an entirely lossless circuit

element.

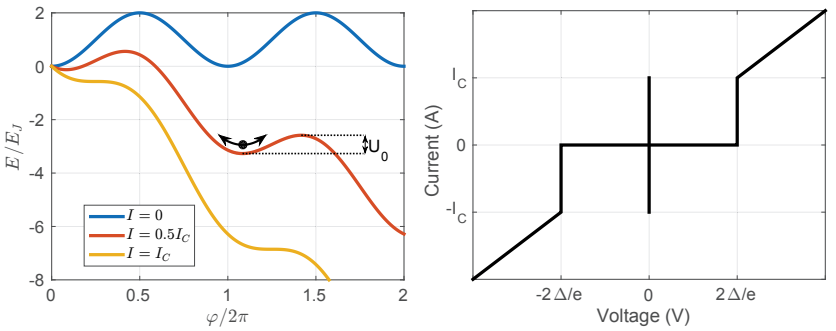

(a) **(b)**

Figure 2.2. a) Phase particle in washboard potential, a mechanical analogue used within the context of the Resistively and Capacitively Shunted Junction (RCSJ) model [5]. b) Current-voltage characteristics of a Josephson junction in idealised noiseless environment.

The basic equations [6] governing the dynamics of Josephson junctions are 1) the superconducting phase evolution equation (AC Josephson relation)

$$2eV = \hbar \frac{\partial \phi}{\partial t} \tag{2.1}$$

and 2) the weak-link current-phase relation (DC Josephson relation)

$$I = I_C \sin(\phi). \tag{2.2}$$

Combining Eq. 2.1 with the derivative of Eq. 2.2, we obtain $V = \frac{\phi_0}{2\pi I_C \cos(\phi)} \frac{\partial I}{\partial t}$. This is of the same form as the definition of inductive voltage. Using Eq. 2.2 and $\cos(\phi) = \sqrt{1 - (I/I_C)^2}$, a JJ can be considered an inductor with

$$L_J = \frac{\phi_0}{2\pi I_C \sqrt{1 - (I/I_C)^2}}. \tag{2.3}$$

for small currents below the critical current. Here $\phi_0 = \frac{h}{2e} \approx 2.07 \times 10^{-15}$ Tm^2 is the magnetic flux quantum.

The AC Josephson effect occurs when fixed voltage is applied to the junction. As a result, an AC current with amplitude I_C and frequency $\frac{2e}{h} V_{DC}$ will flow in the junction. In the inverse AC Josephson effect a well defined voltage will appear across the junction under AC exitation. This phenomenon is employed as a voltage standard.

2.2 Superconducting Quantum Interference Device

A loop made of superconducting material interrupted by JJs is called a superconducting quantum interference device (SQUID). The magnetic flux enclosed by any superconducting loop must be an integer number of flux quanta $\phi = n\phi_0$. If an external flux is applied, there will be a screening current which exactly cancels the external flux. The critical current oscillates as depicted in Fig. 2.4b. At $\phi = n\phi_0 + \frac{1}{2}\phi_0$ it becomes energetically favourable for the SQUID to change the direction of the screening current.

Typically, two JJs are embedded into a SQUID loop in which case the device is called a DC-SQUID.

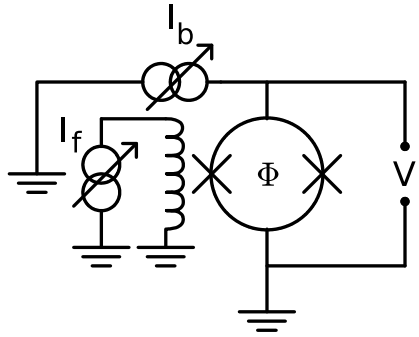

Figure 2.3. Biasing a SQUID with current I_b above the critical current will result in voltage V across the SQUID. Changing the current I_f to external coil will attemp to change the flux Φ through the SQUID and will result in modulation of the effective critical current $2I_C^0$ of the SQUID.

The effective critical current of a single idealized DC-SQUID is

$$I_C = 2I_C^0|\cos(\pi\Phi/\Phi_0)|, \tag{2.4}$$

where I_C^0 is the critical current of a single junction in the SQUID, Φ/Φ_0 is the magnetic flux enclosed by the SQUID loop in units of flux quanta. This formula is valid for small loop inductances. The loop sizes used in the experiments presented in this thesis are minimized and the geometric inductance of the loop can be mostly ignored only contributing by slightly lowering the resonant frequency of the devices. Both junctions are assumed identical. This modulation of the effective critical current allows the effective inductance of the SQUID to be modulated by external flux as in the case of current modulating that of a single junction. This inductive modulation is used throughout the publications presented in this thesis.

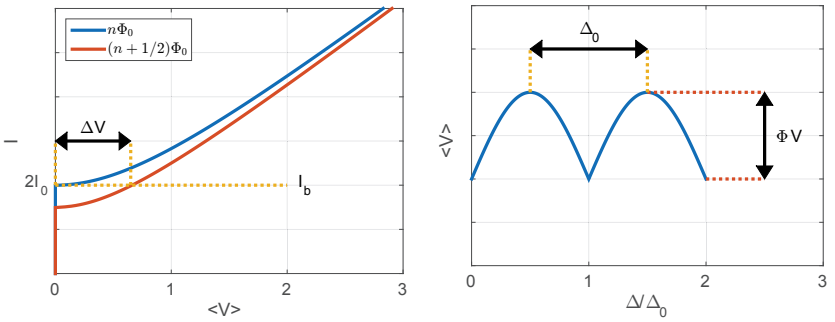

(a) **(b)**

Figure 2.4. a) IV-curve of resistively shunted SQUID with two different flux biases. Modulation of the external flux will result in modulated IV-curve for the SQUID and for current I_b shall result in modulation of voltage ΔV across the SQUID. b) Visualization of ΔV as a function of external flux bias.

A DC-SQUID can also be used as a magnetometer. This is done by current biasing the SQUID on a point with steep linear slope in its flux to voltage curve.

2.3 Quantum vacuum

The quantum noise studied in this thesis is typically considered to originate from resistors or semi-infinite transmission lines. However, in general the origin of this noise is considered to be dissipation or vacuum.

Terms such as quantum fluctuation, virtual particles, vacuum energy, zero-point energy, zero-point motion, and ground state energy are also used. These are all consequences of the non-commuting nature of conjugate pairs of quantum observables. Heisinberg's uncertainty principle

$$\Delta x \Delta p \geq \frac{\hbar}{2} \tag{2.5}$$

states that there is a certain fundamental limit to the precision at which these pairs of conjugate variables, such as position x and momentum p, can be known. Similar uncertainty relations exist for many other pairs of observables, including time & energy, number of charge carriers & phase and the orthogonal quadratures of the electromagnetic field I & Q. Perhaps the most tangible manifestation of quantum noise is shot noise in single photon detectors which, rather than displaying a continuous reading, are like Geiger counters which detect clicks corresponding to the ar-

rival of an energy packet - a photon.

As for visible light, photons exist also for microwaves and indeed for all frequencies of the electromagnetic spectrum. In contrast to the frequency of visible light which is on the order of $5 \times 10^{14}\mathrm{Hz}$, the microwave frequencies in our experiments are on the order of $5 \times 10^{9}\mathrm{Hz}$. Energy of a single photon in Kelvin (K) is $E = \frac{\hbar\omega}{k_b}$. For visible light the photon energy is 20 000 K making it relatively easy to have detectors whose internal noise contribution ($\approx$ 100 K) is significantly less than this energy and they can efficiently work as single photon detectors. The energy of microwave photons is in the range of 1 K.

Quantum effects become dominant in the limit of $T \to 0$, where the necessary temperature depends on the frequency ($\hbar\omega \gg k_b T$) to avoid thermal noise. Void of interfering mechanisms like mixing by nonlinearities, the quantum noise of a resistor (in an optimally coupled circuit) has a power spectral density of the form

$$S_q = \frac{\hbar\omega}{2}. \tag{2.6}$$

At non-zero temperature we can calculate the power spectrum by combining Planck's law with the quantum noise relation, which yields the Callen-Welton formula [7]

$$S_n = \hbar\omega \left(\frac{1}{e^{\hbar\omega/k_B T} - 1} + \frac{1}{2} \right). \tag{2.7}$$

Experiments in this thesis are mostly done at the limit ($\hbar\omega \gg k_b T$) where the effect of temperature is insignificant [8].

In this thesis, the central pair of non-commuting observables are the field quadratures I and Q. These are related to the field operators [9] by

$$I = \frac{1}{2} \left(a_{out} + a_{out}^{\dagger} \right) \tag{2.8}$$

and

$$Q = \frac{1}{2i} \left(a_{out} - a_{out}^{\dagger} \right). \tag{2.9}$$

The commutation relation between I and Q is

$$[I, Q] = \frac{i}{2}. \tag{2.10}$$

However, one should keep in mind that our measurements are performed with noisy amplifiers which add noise on the order of 20 photons into the measurement data. Consequently, the actual measurements are performed over long averaging times. From the point of view of the theoretical introduction, we can ignore this here since the amplifier noise is simply an uncorrelated, well behaving source of noise.

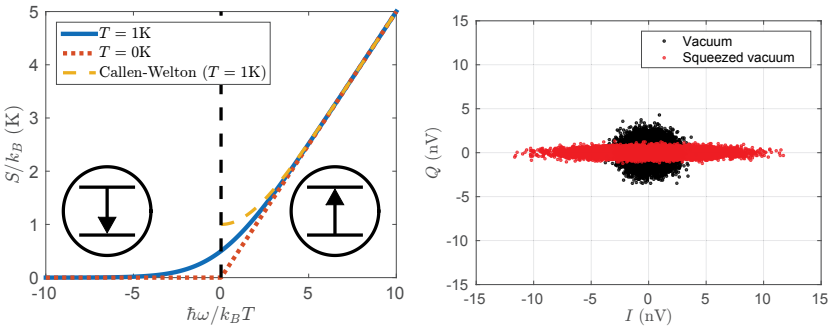

(a) **(b)**

Figure 2.5. a) Emission ($\omega < 0$) and absorption ($\omega > 0$) spectra. Notice that the emission and absorption always sum up to the Callen-Welton form. b) Quadrature plot of the standard vacuum state and squeezing of one quadrature below the vacuum value (squeezed vacuum). Squeezing implies correlation of the sidebands (relative to ω). Squeezing below the vacuum value implies that if the sidebands were subtracted from each other the remaining value would be less than vacuum noise.

A time domain signal $x(t)$ can be perfectly described by its quadrature form

$$x(t) = I(t)\cos(\omega t) + Q(t)\sin(\omega t), \tag{2.11}$$

which can be conveniently expressed in a complex form

$$f(t) = I(t) + iQ(t). \tag{2.12}$$

The quadratures I and Q are orthogonal to each other which means that

the information they carry can be independent and uncorrelated. Instantaneous power of a quarature signal is proportional to $|I|^2+|Q|^2$, and the instantaneous phase angle of the signal can be easily calculated by $\varphi = \arg(z = I + iQ) = \arctan(I/Q)$.

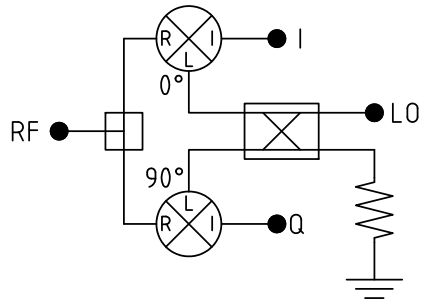

Figure 2.6. Block diagram for a standard IQ-mixer.

The time domain quadrature data may be converted into frequency spectrum around ω by the Fourier transform

$$F(\omega) = \int_{-\infty}^{\infty} f(t)e^{-i\omega t}dt. \tag{2.13}$$

Fast Fourier transform (FFT), which is the numerically efficient algorithm for the discrete Fourier transform (DFT), was extensively utilized in analyzing the data in Publication V. Processing the data in Fourier-transformed format, i.e. in amplitude-phase form is especially convenient for calculating correlation by splitting the data to different frequency ranges of interest as well as analyzing the phase angle dependencies of the correlations.

2.4 Quantum amplifiers

A device where a signal is amplified by modulating some system parameter, such as its natural resonant frequency, by an external power source is called a parametric amplifier. In the electrical systems, typically, some reactive element of a lossless circuit is modulated by a pump at 2ω, thereby resulting in gain at ω. In our samples, we modulate the effective inductance of SQUIDs by external flux.

The lowest-order approximation of the Hamiltonian for a modulated cavity is

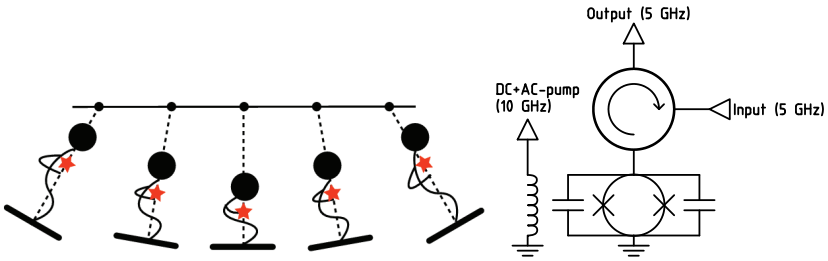

Figure 2.7. a) A parametric resonance in a swing driven by a person [10] varying the center of mass at twice the natural resonant frequency of the system. Driving below oscillation threshold will amplify small variations in the fluctuations of the swing. b) The principlal components of a simple parametric amplifier. The SQUID inductance is pumped at 2ω by the coil on the left while being tuned to the desired resonant frequency at ω by the DC-component. Input signal at ω is fed through the circulator, experiences reflection gain and exits through the third port of the circulator.

$$H = \hbar\omega_{res}a^\dagger a + \frac{\hbar}{2}\left[\alpha^* e^{i\omega_p t} + \alpha e^{-i\omega_p t}\right](a + a^\dagger)^2. \tag{2.14}$$

Here ω_{res} is the resonant frequency of the cavity, the cavity is pumped by $\omega_p = 2\omega_{\mathrm{res}}$, α is the pumping strength and a is the cavity mode. Time dependence can be removed by moving to a rotating-frame of ω by transformation $U = e^{i\omega_{\mathrm{res}}a^\dagger a t}$. The transformed Hamiltonian is then $H = i\hbar\dot{U}U^\dagger + UHU^\dagger$. The rotating wave approximation becomes $H_{RWA} = -\frac{\hbar}{2}[\alpha^* a^2 + \alpha(a^\dagger)^2]$.

The Heisenberg-Langevin equations are then

$$\dot{a} = \frac{i}{\hbar}[H_{RWA}, a] - \frac{\kappa}{2} - \sqrt{\kappa}a_{in}, \tag{2.15}$$

or

$$\dot{a} = i\alpha a^\dagger - \frac{\kappa}{2} - \sqrt{\kappa}a_{in}, \tag{2.16}$$

$$\dot{a^\dagger} = -i\alpha a - \frac{\kappa}{2} - \sqrt{\kappa}a_{in}^\dagger. \tag{2.17}$$

A Fourier transform yields

$$\begin{pmatrix} \chi^{-1}(\xi) & -i\alpha \\ i\alpha^* & \chi^{-1}(\xi) \end{pmatrix} \begin{pmatrix} a(\xi) \\ a^\dagger(\xi) \end{pmatrix} = -\sqrt{\kappa} \begin{pmatrix} a_{in}(\xi) \\ a_{in}^\dagger(\xi) \end{pmatrix} \tag{2.18}$$

Here $\chi = \frac{1}{\kappa/2 - i\xi}$ is the electrical susceptibility of the resonator, κ is the cavity decay rate, α denotes a parameter proportional to the pump amplitude and ξ any frequency in the vicinity of ω_{res}.

Using input-output relations we write

$$a_{out}(\xi) = a_{in}(\xi) + \sqrt{\kappa} a(\xi), \tag{2.19}$$

and the output field becomes

$$a_{out}(\xi) = \left(1 - \frac{\kappa\chi(\xi)}{\mathcal{N}(\xi)}\right) a_{in}(\xi) - \frac{i\alpha\kappa}{\mathcal{N}(\xi)} \chi(\xi)\chi(-\xi)^* a_{in}(-\xi)^\dagger. \tag{2.20}$$

Here $\mathcal{N}(\xi) = 1 - \alpha^2\chi(\xi)\chi(-\xi)^*$ is an auxiliary variable (responsible for gain).

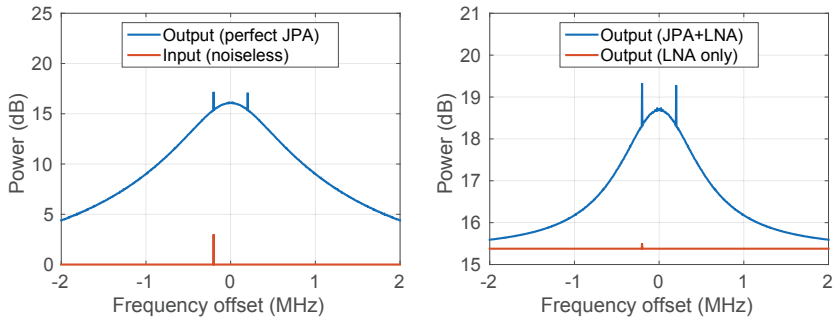

(a) **(b)**

Figure 2.8. a) Spectrum of an ideal input signal (vacuum noise and $\hbar\omega$-level signal) and output of a perfect JPA with that input. Idler generation is seen as a mirror image of power with respect to the center in the spectrum. S/N is degraded by an amount corresponding to quantum limit. b). Illustration of how the signal from a) would look like in a real system amplified with a typical LNA with a gain of 40 dB and noise temperature $T_N = 17\hbar\omega$ (4.1 K @ 5 GHz).

The performance of all amplifiers, including parametric amplifiers, can be characterized by noise temperature. It is a measure of the amount of noise power the amplifier adds to the measured input signal while amplifying it. Noise temperature is expressed in Kelvins. An ideal classical amplifier has a noise temperature of $T_N = 0$ K. However, all practical amplifiers when operated in phase-insensitive mode in the limit of high gain, are limited by the Heisenberg uncertainty principle [11] and thus can only approach a minimum noise temperature of $T_Q = \frac{\hbar\omega}{2k_B}$, which is called the standard quantum limit (SQL) for amplifier noise. For exam-

ple at 5 GHz, a frequency of interest in our measurements, this value is around 120 mK.

The SQL of amplifier noise is specified by the Haus-Caves theorem

$$\frac{(\Delta\hat{a}_{\rm out})^2}{G} \geq (\Delta\hat{a}_{\rm in})^2 + \frac{1}{2} - \frac{1}{2G}. \tag{2.21}$$

Here, $\hat{a}_{\rm out} = \sqrt{G}\hat{a}_{\rm in} + \hat{\mathcal{F}}$, where $\hat{a}$ is the mode to be amplified and $\hat{a}_{\rm out}$ denotes the output mode. $\hat{\mathcal{F}}$ represents the noise which gets added to satisfy the commutation relations $[\hat{a}_{\rm in}, \hat{a}^\dagger_{\rm in}] = [\hat{a}_{\rm out}, \hat{a}^\dagger_{\rm out}] = 1$.

The theorem can be shown as follows. By definition $(\Delta\hat{a}_{\rm out})^2 \equiv \frac{1}{2}\langle\{\hat{a}_{\rm out}, \hat{a}^\dagger_{\rm out}\}\rangle - |\langle\hat{a}_{\rm out}\rangle|^2 = \frac{1}{2}\langle(\sqrt{G}\hat{a}_{\rm in}+\hat{\mathcal{F}})(\sqrt{G}\hat{a}^\dagger_{\rm in}+\hat{\mathcal{F}}^\dagger)+(\sqrt{G}\hat{a}^\dagger_{\rm in}+\hat{\mathcal{F}}^\dagger)(\sqrt{G}\hat{a}_{\rm in}+\hat{\mathcal{F}})\rangle - (\sqrt{G}\langle\hat{a}_{\rm in}\rangle + \langle\hat{\mathcal{F}}\rangle)(\sqrt{G}\langle\hat{a}^\dagger_{\rm in}\rangle + \langle\hat{\mathcal{F}}^\dagger\rangle)$. The uncorrelated nature of the idler fields with the input means $[\hat{a}_{\rm in}, \hat{\mathcal{F}}] = [\hat{a}_{\rm in}, \hat{\mathcal{F}}^\dagger] = \langle\hat{a}_{\rm in}\hat{\mathcal{F}}\rangle = \langle\hat{a}_{\rm in}\hat{\mathcal{F}}^\dagger\rangle = 0$. Therefore we get $(\Delta\hat{a}_{\rm out})^2 = G(\Delta\hat{a}_{\rm in})^2 + \frac{1}{2}\langle\{\hat{\mathcal{F}}, \hat{\mathcal{F}}^\dagger\}\rangle \geq G(\Delta\hat{a}_{\rm in})^2 + \frac{1}{2}|\langle[\hat{\mathcal{F}}, \hat{\mathcal{F}}^\dagger]\rangle|$. The commutator $[\hat{a}_{\rm out}, \hat{a}^\dagger_{\rm out}] = 1 = G + [\hat{\mathcal{F}}, \hat{\mathcal{F}}^\dagger]$, leading to $[\hat{\mathcal{F}}, \hat{\mathcal{F}}^\dagger] = 1 - G$ which, together with the previous results, yields the Haus-Caves theorem [12].

2.5 Noise temperature

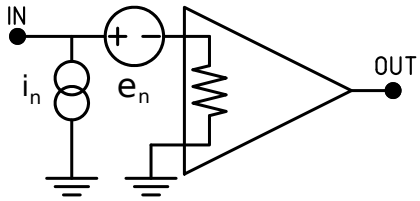

Figure 2.9. Amplifier noise model separating the input current and voltage noise sources. For an amplifier in a matched environment (with circulators for example) it is sufficient to consider only one effective matched noise source such as only the current source parallel to the input. However, in an unmatched case the full model must be employed.

The total noise temperature of an arbitrary system with several amplifiers with their respective noise temperatures T_n and gains G_n is given by the Friis formula [13]. Clearly, if the first amplifier has a large enough gain relative to T_2/T_1, its noise temperature dominates the total system noise temperature:

$$T_{system} = T_1 + \frac{T_2}{G_1} + \frac{T_3}{G_1 G_2} + ... + \frac{T_N}{G_1 G_2 ... G_{N-1}}. \tag{2.22}$$

One should keep in mind that, when amplifying standard signals from quantum vacuum, the total noise of a quantum limited low noise amplifier (LNA) equals $\frac{\hbar\omega}{k_B}$ (in the limit of high gain), which is due to the fact that half of the noise originates from the vacuum itself while the other half comes from the amplification process. When using phase sensitive amplifiers, the situation may change from the perspective of a single quadrature as the vacuum can be squeezed to contain less noise in one quadrature at the expense of the other one, and the amplifier may amplify a single quadrature in a noiseless way. Even the phase insensitive amplifier can be considered noiseless in the sense that it doesn't add noise from any external sources, but the reduction in ideal S/N corresponding to the quantum noise originates rather from the process of mixing of quantum noise between the upper and lower sideband (relative to ω). Interestingly, this process is reversible as the amplifier performs a unitary transformation. Since there is no loss of information, restoration of the original unamplified state is possible. However, this is true only for dissipationless devices, i.e. when all stochastic elements are absent.

Noise temperature of an amplifier is commonly determined by the Y-method. The method uses a known variable source of noise, such as a heated resistor or a normal tunnel junction, which provide thermal and shot noise, respectively. Varying the noise power at the input and recording the power at the output of the amplifier yields a straigth line which can be extrapolated to a point where the input noise source would provide no noise at all. This point gives the noise temperature of the amplifier.

Voltage biased normal tunnel junction will produce shot noise which at zero temperature and zero frequency has a power spectral density $\langle \delta i^2 \rangle$ of $S_P = 2e|I|$. For nonzero temperature and frequency the noise takes the following form [14]:

$$S(f,V,T) = \frac{2k_BT}{R}[\frac{eV+hf}{2k_BT}\coth(\frac{eV+hf}{2k_BT}) + \frac{eV-hf}{2k_BT}\coth(\frac{eV-hf}{2k_BT})]. \tag{2.23}$$

Shot noise in a regular tunnel junction originates from the current consisting of discrete charge carries. The number of electrons crossing the barrier over a period of time follows Poisson statistics. Consequently, with reference to Poissonian noise S_P, a tunnel junction can be described by a constant Fano factor of $F = S/S_P = 1$. It can be used as a known noise reference for calibrating the amplifier noise temperature (or for extract-

ing a Fano factor of an unknown sample).

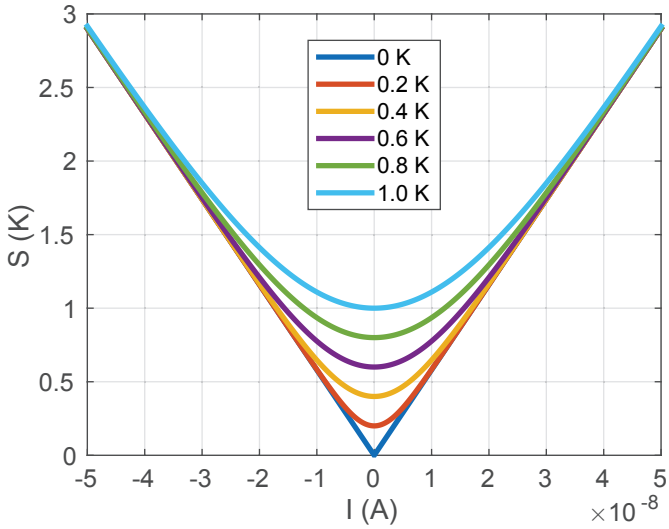

Figure 2.10. Noise of a voltage biased normal tunnel junction as a function of current. The curves are calculated at $\omega = 0$ for a fully matched source-load system at temperatures indicated in the figure.

3. Superconducting Josephson Junction based devices

This section gives an overview of Publications I, II and V which all fall into the same category, concerning Josephson junction based devices and noise in them. Publication I is discussed in Sect. 3.1, Publication II in Sect. 3.2 and Publication V in Sect. 3.3.

3.1 Negative resistance single junction amplifier

The general principle behind the single junction amplifier (SJA) is the negative differential resistance provided by the DC-biased JJ. This is easily seen by considering the current-voltage characteristics of resistively shunted JJ. A junction with a critical current of I_C when biased with a current I_b has the following current-voltage (IV) characteristics

$$< V >= R\sqrt{I_b^2 - I_C^2}, \tag{3.1}$$

which can be derived from Eq. 2.1, 2.2 and Kirchhoff's circuit laws. The result is plotted in Fig. 3.1b in blue. By subtracting the linear resistive component (dashed yellow line), we obtain the IV with differential resistance $R_d = \frac{\partial <V>}{\partial <I>} < 0$ for a standalone junction (in red). The negative differential resistance is a result of the high frequency phase dynamics and is valid only for frequencies well below the Josephson frequency.

The regular reflection coefficient

$$\Gamma = \frac{Z - Z_0}{Z + Z_0}, \tag{3.2}$$

is valid also at $Z < 0$ and the subsequent power gain is $G = |\Gamma|^2$; for negative values of Z, the gain diverges to infinity when $Z \to -Z_0$.

The gain of the SJA ultimately derives its energy from the DC-bias driven high frequency dynamics. The nonlinearity of the JJ and the Josephson oscillations in turn makes it possible to mix signal power up and down in frequency, producing gain through this mixing process. Hence, we can consider the SJA as a special case of parametric amplifier which is operated by a self-generated pump at the Josephson frequency.

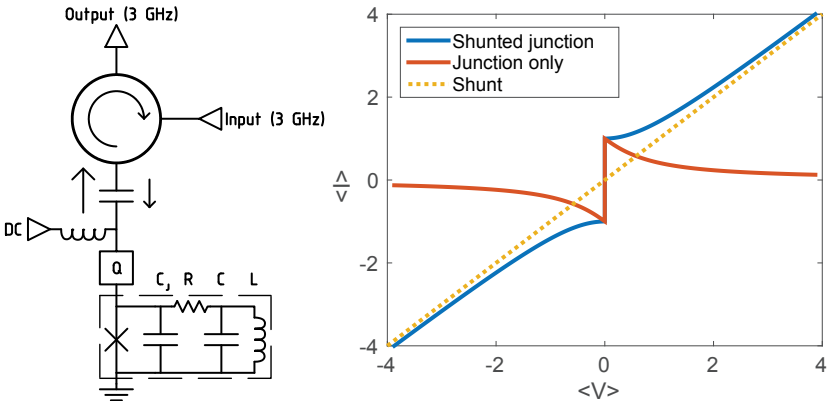

Figure 3.1. a) Schematic for the standard measurement setup for using the SJA with the on-chip circuit depicted in dashed box. b) IV-curves for the resistively shunted junction, a standalone junction and the junction shunt. Units are specified by $R = I_C = 1$. Biasing to the negative slope allows reflection gain to be obtained from the device.

Circuit parameters, such as the characteristic environment impedance $Z_0 = 50\Omega$ and bandwidth limitations, do not allow a single JJ to be operated as an amplifier directly because the negative slope of the IV-curve is inherently unstable. To access the regime $\frac{dI}{dV} < 0$, the device must be stabilized by properly engineering the impedances around it. To this end, we divide the environment into two separate frequency ranges, the signal band and the off-signal band. They are damped separately: signal band is damped by the environment impedance which is further impedance matched to the JJ by a matching network, depicted in Fig. 3.1a by Q. The off-signal band is damped by an on-chip resistor. The on-chip resistor is prevented from damping the signal band by a bandstop filter, in our case a basic LC-circuit.

The bandstop filter has the additional benefit of simultaneously blocking the Johnson noise of the shunt from entering the system at the signal frequency. Theoretically, the only path for the noise in our device is the high frequency dynamics i.e. the down mixing of quantum noise of the on-chip shunt at the Josephson frequency.

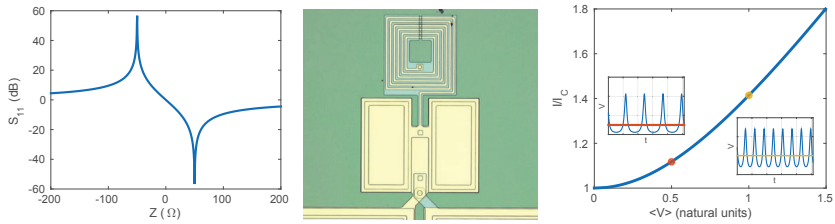

Figure 3.2. a) Reflection S_{11} in a $Z_0 = 50\Omega$ environment from impedance Z allows gain to be obtained at negative impedance values. This gain diverges to infinity at $Z = -Z_0$. The dramatic property of ideal negative resistance is that it allows infinite bandwidth. In the experiment presented in this thesis the bandwidth is, however, restricted by the on-chip bandpass filter. This filter is at the same time partly responsible for the good noise performance. Practical systems are in addition limited by stability conditions and high frequency dynamics, etc. b) Micrograph of the actual sample. The field of the image is roughly to 270 $\mu m \times$ 230 μm. c) Short time solution based on Eq. 2.1 and 2.2 displaying the high frequency dynamics along the IV-curve responsible for the generation of the mean voltage values $\langle V \rangle$ of the R-shunted junction for biases above I_C in an ideal circuit ($I_C = 1, R = 1$ at $\omega \ll \omega_J$).

Experimentally we obtained a gain of 28 dB with -3 dB bandwidth of 1 MHz. The -1 dB compression point P_{in} was -134 dBm. These values are mainly set as a result of the circuit parameters and stability conditions.

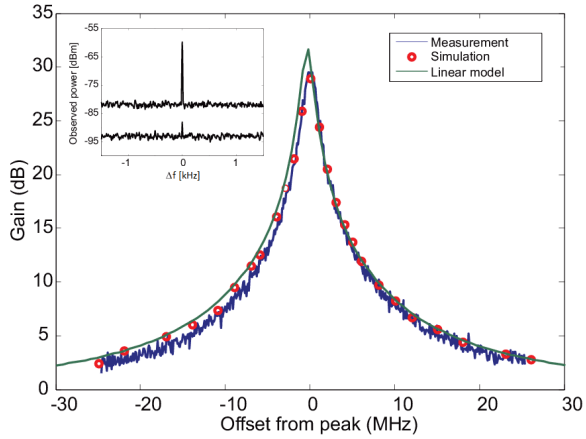

Figure 3.3. The experimentally observed gain along with the best observed S/N improvement by the SJA.

The lowest added noise was found to be $T_N = 1.6\hbar\omega$, which was initially unexpected as the linear noise model predicted 17 quanta. This value is comparable to other near-quantum limited implementations [16–27]. This discrepancy was numerically explained by the power contained in the wideband noise which alters the Josephson phase dynamics in a way

which reduces the mixed down noise without equal degradation in the gain. The operating point for this "self organizing" is sensitive and requires sufficient gain and bandwidth to become realized.

3.2 Dynamical Casimir effect

The dynamical Casimir effect occurs when the boundary conditions of a region of vacuum are changed rapidly [28–34]. Typically this is depicted as a mirror moving in vacuum. This has the consequence of converting vacuum fluctuations into real photons. These photons are generated in pairs whose sum frequency matches that of the modulation frequency of the mirror. This pairwise creation can be detected by measuring the correlation of the emerging photons.

Similar effects due to vacuum fluctuations, such as the electron-positron pair production in intense electrical field (Schwinger effect), evaporation of black holes (Hawking radiation), and observation of thermal radiation by an accelerating observer (Unruh effect), are predicted to occur as well. Several proposals for observing such effects [35–47] have been suggested.

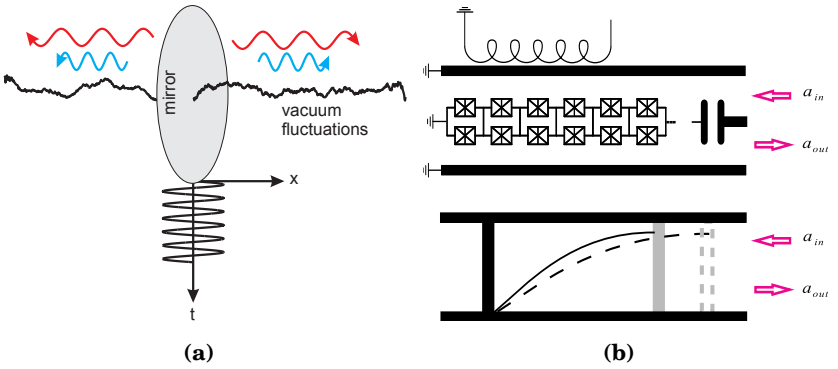

Figure 3.4. a) A mirror moving in vacuum will create photon pairs (blue and red wavy lines) from vacuum fluctuations (in black). b) Illustration of the actual sample circuitry along with its mechanical analogue.

Moving a mechanical mirror literally at a rate large enough to create detectable amounts of radiation has so far been impossible due to the necessary relativistic velocities. If the mirror is not moving fast enough, the vacuum field can adiabatically adapt to the changes of the boundary condition and no excitation occurs. However, in our experiment we operate an electrical analogue by changing the index of refraction of a cavity. This is accomplished by modulating the inductive component of the unit cells in our JJ metamaterial cavity. Our unit cell is comprised of a SQUID,

and as described in Sect. 2.2, their inductance depends on the magnetic flux. This way the effective boundary condition can be modulated at a rate which corresponds to a significant proportion of the speed of light. The cavity itself also acts as a means of increasing the generated photon flux, making the detection of the generated photon pairs easier.

Traditionally, frequency-correlated photons are generated by nonlinear effects [48, 49]. The DCE occurs due to mismatch between the field modes at different times when the vacuum is perturbed fast enough. In our case, this perturbation is accomplished by changing the index of refraction of the metamaterial cavity fast enough (while still keeping the modulation linear).

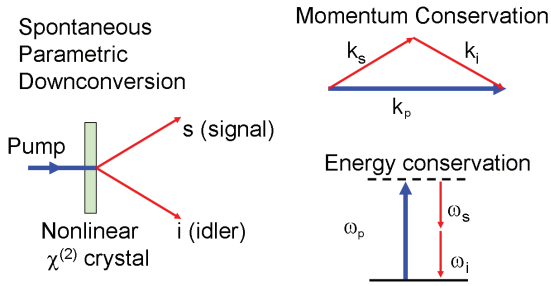

Figure 3.5. Spontaneous parametric down conversion in optics [15]. A high energy photon fired at a nonlinear crystal is downconverted by the crystal into two entangled photons of lower energy so that the total energy and momentum is conserved. This process is seeded by vacuum fluctuations.

The dynamical Casimir effect under parametric pumping is equivalent to parametric amplification of vacuum fluctuations to spontaneous parametric down conversion of a pump photon at 2ω down to two around ω as depicted in Fig. 3.5; ω_s and ω_i do not need to be equal, but $\omega_s + \omega_i = \omega_p$.

The input-output relation in Eq. 2.20 for the parametric amplifier can be broken further down into internal and external decay rates. This is important when analyzing nonidealities of the actual samples and making sure that the modulation acts on the vacuum ground state rather than on some thermally excited state.

Perhaps the most counterintuitive aspect of this experiment is that the device and its microwave environment is cooled down to near zero temperature and, as such, one might classically expect it to be unable to yield any detectable signals. Therefore the observation of correlated photon pairs emanating from the sample is in agreement with the quantum mechanical prediction. It is important to stress that energy is conserved in

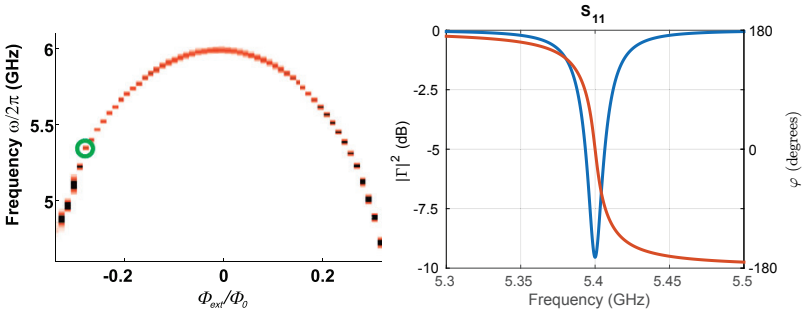

(a) **(b)**

Figure 3.6. Essential characteristic of the DCE sample is the tunability of the electrical resonance quickly tunable by flux (the current supplied to the on-chip coil). This effect is demonstrated in a) where ω_{res} is modulated. Plotted is S_{11} where the peak of the resonance is seen in red/black. b) Typical S_{11} for the resonator where the amplitude of the reflection is shown in blue and phase in red.

this process. The observed energy ultimately originates from the down-converted pump.

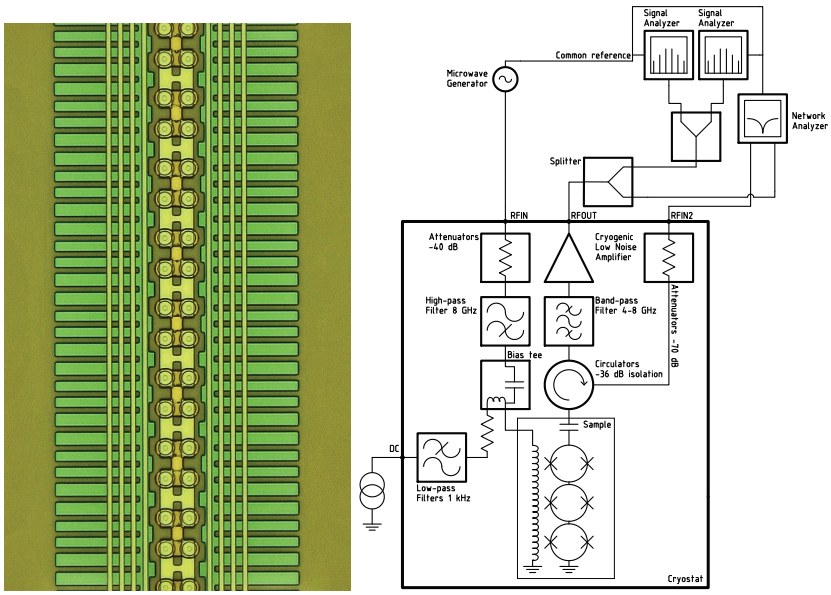

(a) **(b)**

Figure 3.7. a) Optical micrograph of our metamaterial sample. The unit cell consisting of two SQUID loops is repeated 125 times constituting a cavity whose resonant frequency can be tuned between 5-6 GHz. b) Measurement schematic used for experiments presented in Publication II.

By observing symmetric bimodal spectra of generated photons when the cavity resonance is detuned away from half of the pump frequency allows us to be confident that no significant heating of the internal modes occurs

in our system. Thermal excitation of photons could result in classical signatures similar to the DCE.

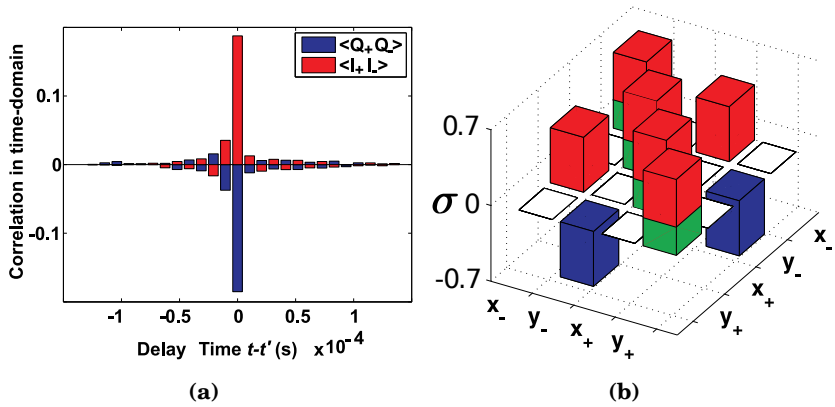

Figure 3.8. a) Observed cross-correlations for the in-phase (I) and quadrature (Q) amplitudes. b) Covariance matrix $\sigma(A,B) = \frac{1}{2}\langle\{A,B\}\rangle$, where $\{,\}$ denotes anti-commutator. The standard vacuum power is marked in green. The nonzero off-diagonal elements indicate the squeezing correlations. The orthogonal quadratures x and y of the lower (-) and upper (+) sidebands are $x_\pm = (1/2)(a_\pm + a_\pm^\dagger)$ and $y_\pm = (1/2i)(a_\pm - a_\pm^\dagger)$. This covariance matrix satisfies the nonseparability condition $\sigma(x_+,x_+) - \sigma(x_+,x_-) < 1/4$.

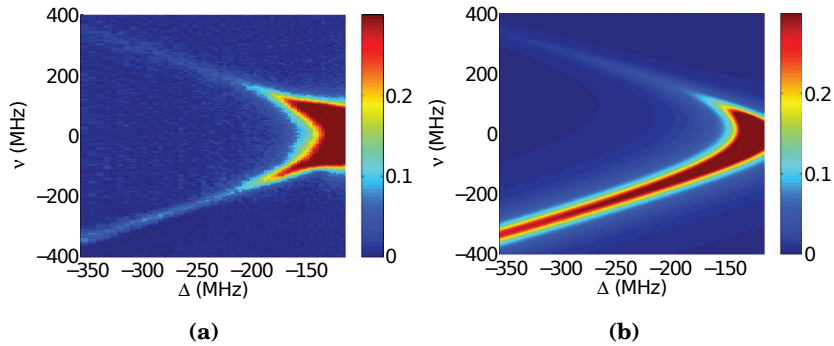

Figure 3.9. a) Emitted noise as a function of frequency measured in the vicinity of $\omega_p/2$ while tuning $\omega_{\rm res}$ at constant pump power. b) Theoretical prediction for overheated internal modes with a single quantum of classical noise. It is evident that the result on the left matches better the quantum mechanical prediction without overheating.

The sample was also characterized by measuring the standard scattering parameters in order to obtain the internal and external cavity decay rates. Using the definition of χ, the reflection coefficient becomes $\Gamma = 1 - \kappa_e\chi$ and $\kappa = \kappa_i + \kappa_e$. A network analyzer can be used to measure $|S_{11}| = 10log_{10}|\Gamma|^2$ (dB) and $Arg(S_{11})$, which can be employed to solve for κ_i and κ_e.

For this experiment we had $Q \approx 100$ and $\kappa_e \approx 2\kappa_i$; the corresponding

scattering parameters are given in Fig. 3.6. It is important that external decay rate dominates the internal one because is essential to minimize internal dissipation if squeezing of the external vacuum is desired. Noise temperature is also affected by internal dissipation if the device is operated as a parametric amplifier.

If the value of the off-diagonal element $\sigma(x_+, x_-)$ (in Fig. 3.8b) reaches close to the total diagonal amplitude $\sigma(x_+, x_+)$, such that $\sigma(x_+, x_+) - \sigma(x_+, x_-) < 1/4$, the vacuum level has been squeezed (along a single quadrature). This means that two parts of the perturbed vacuum have acquired so high correlation that their interference (for example after homodyne detection) would yield less noise than the standard vacuum (in one quadrature) [50–53]. Our best value was $\sigma(x_+, x_+) - \sigma(x_+, x_-) = 0.18 \pm 0.01$. Assuming Gaussian states, this corresponds to a logarithmic negativity $E_N = 0.32$ and to an entropy of formation $E_F = 0.125$ entangled bits, where $E_F = \frac{Tr[\sqrt{\sigma^\dagger \sigma}]-1}{2}$ and $E_N = \log_2(2E_F + 1)$.

Measurement of the correlation between the generated photon pairs was done by capturing the I/Q signals by digitizing the two separate frequencies, symmetrically located with respect to half of the pump frequency. Due to software and data transfer related limitations, two analyzers were used initially instead of one. If the relevant signal is within the digitization bandwidth of one analyzer, then a single analyzer is sufficient (as was done in Publication V). All the devices were supplied with a common frequency reference and the capture of the analyzers was triggered simultaneously. This method relies on the fact that the preamplifier noise at different frequencies is uncorrelated. This was carefully checked prior to the experiments and no correlation could be detected.

A careful calibration of certain quantities in the measurement system is needed. In particular, the noise levels of the system must be known to sufficient precision. Perhaps the most important single quantity needed is the noise temperature of the preamplifier. This has to be known with a good precision because it is used to determine the power level corresponding to vacuum noise. Standard thermal Y-method and a correlation method was used to verify the noise temperature of the preamplifier(s). In the Y-method the source temperature is varied while the amplifier temperature is kept constant. This method is accurate as long as the amplifier gain doesn't drift significantly while the source temperature is varied. In addition to this, a correlation technique where a thermal signal is fed into a splitter (or -3 dB coupler) thermalized to a fixed temperature is con-

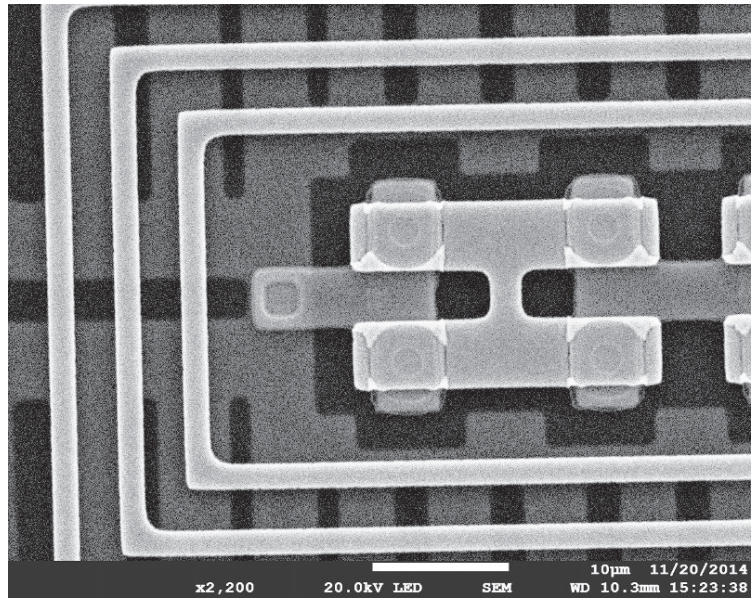

Figure 3.10. Scanning electron micrograph of the grounded end of the junction chain showing two SQUID loops in the H-type structure.

nected into two amplifiers. Power levels can be deduced from the correlation spectrum corresponding to the quantum noise floor. The correlation method is significantly less sensitive to amplifier gain drift than direct power measurement.

While measuring the power levels of the generated DCE photons, the zero level was constantly monitored by switching the pump power on and off. This allowed the difference from the vacuum level to be know to good precision and helped to eliminate problems associated with the preamplifier gain drift.

Since the preamplifier gain compression caused by a strong pump signal can act as a source of squeezing-like signals, we eliminated this possibility by checking separately that there is no gain compressed present with the used pump powers. This is done by measing the amplifier gain off-resonance with the pump on and off.

Serious difficulty is relate to the phase drift of microwave generators and phase-sensitive detectors with respect to each other. This is especially important when measuring squeezing over long averaging times. Too much drift will eliminate the squeezing correlation and make it appear as if no squeezing occurs. This problem can be compensated by averaging only for short time windows during which the phase doesn't have enough time to drift significantly. However, this is not always an option.

Another method is to introduce a small reference signal derived from the pump (for example by using a frequency divider) which can then be used to correct the phase drift afterwards.

3.3 Tripartite correlations

The dynamical Casimir effect can be regarded as spontaneous parametric down conversion of a pump photon into two photons, with their energies summing up to the energy of the pump photon. This process is stimulated by vacuum fluctuations - whose existence is a fundamental feature of quantum electrodynamics [54–77]. In Publication V, we used double parametric pumping with small separation between the pump frequencies. One might expect that the down conversion processes can be regarded as random, occuring independently for each pump. In this case, the result would simply be the sum of the two DCE processes. However, it is not the case. One can understand this by a simple intuitive argument: suppose we look at the mode at a certain frequency - then the quantum fluctuations of the mode will trigger two-photon decay in both pumps, resulting in photons at the mirror-image frequencies with respect to half the pump frequencies. These photons will necessarily be correlated, even if they originate from different pumps, due to the fact that they were 'born into existence' by the same quantum fluctuation.

The standard input-output formulas given for a parametric amplifier in Sect. 2.4 are slightly modified due to the presence of two pumps. The full Hamiltonian becomes

$$H = \hbar\omega_{\mathrm{res}} a^\dagger a + \frac{\hbar}{2i} \sum_{p=1,2} \left[\alpha_p^* e^{i\omega_p t} - \alpha_p e^{-i\omega_p t}\right] (a + a^\dagger)^2. \tag{3.3}$$

The Heisenberg-Langevin equations are

$$\dot{a} = -i\omega_{\mathrm{res}} a + \sum_{p=1,2} \left[-\alpha_p^* e^{i\omega_p t} + \alpha_p e^{-i\omega_p t}\right] (a + a^\dagger) - \frac{\kappa}{2} a - \sqrt{\kappa} a_{\mathrm{in}}, \tag{3.4}$$

and the rotating-wave approximation for operator $\tilde{a(t)} = e^{i\omega_{\mathrm{res}} t} a(t)$ is then

$$\dot{\tilde{a}} = \sum_{p=1,2} \alpha_p e^{-2i\Delta_p} \tilde{a}^\dagger - \frac{\kappa}{2} \tilde{a} - \sqrt{\kappa} \tilde{a}_{\mathrm{in}}. \tag{3.5}$$

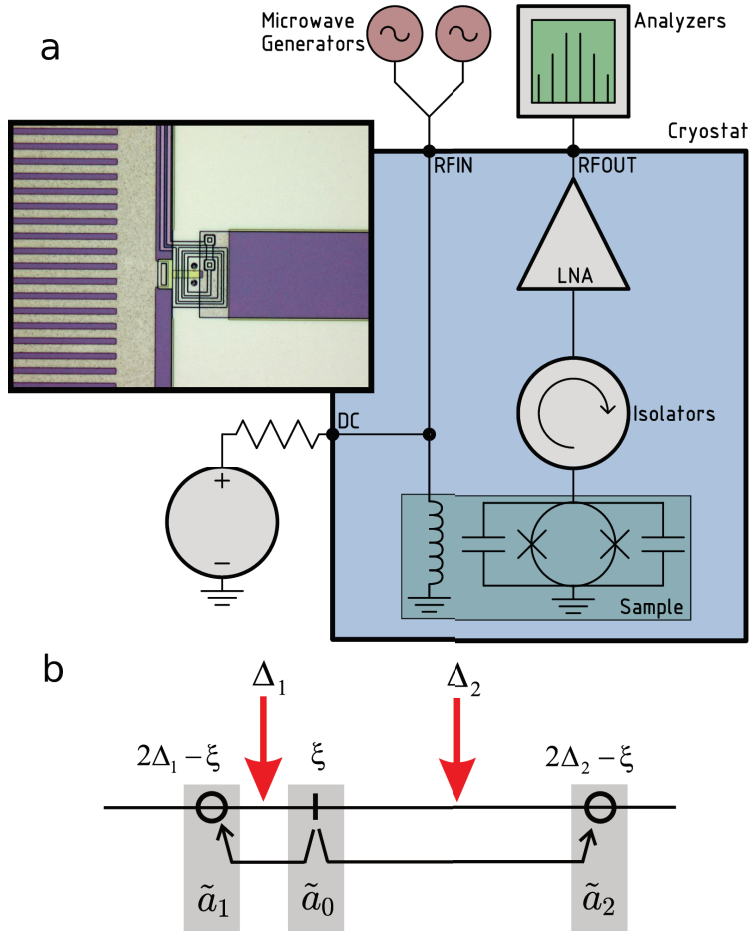

Figure 3.11. a) Simplified schematic of the measurement setup. Micrograph of the sample is depicted in the upper left corner. The investigated resonator consists of a photolithographically fabricated capacitively shunted SQUID. b) Illustration of the first reflections in frequency space with respect to half of the pump frequencies

Here $\omega_1/2\pi$ and $\omega_2/2\pi$ correspond to the two pump frequencies at 10 GHz $\pm$ 10 MHz and $\Delta_p = \omega_p/2 - \omega_{\mathrm{res}}$, where ω_{res} corresponds to the electrical resonant frequency of the resonator. This equation can be solved numerically in time domain (convenient if the pumps have some complicated time dependent envelope) or the whole problem can be analyzed in frequency domain by using the formula for the mode a at frequency $\xi = \omega - \omega_{\mathrm{res}}$.

$$\tilde{a}[\xi] = \frac{\sqrt{\kappa}\chi(\xi)}{1 - \sum_{p=1}^{2} \mathcal{N}_1^{[p]}(\xi)} \left\{ \tilde{a}_{\mathrm{in}}[\xi] + \sum_{p=1}^{2} \frac{\alpha_p \chi^*(2\Delta_p - \xi)}{\mathcal{N}_2^{[p]}(\xi)} \left\{ (\tilde{a}_{\mathrm{in}}[2\Delta_p - \xi])^\dagger + \ldots \right\} \right\} \quad (3.6)$$

Here $\tilde{a}$ corresponds to the field inside the cavity, $\tilde{a}_{\mathrm{in}}$ to the input field and $\tilde{a}_{\mathrm{out}}$ to the output field. One can see that now in the first order, one frequency contains correlated power from the two other frequencies and as a result we see tripartite correlations. The corresponding measurement results and theoretical predictions of the generated noise spectra $\langle \tilde{a}^{\dagger}_{\mathrm{out}} \tilde{a}_{\mathrm{out}} \rangle$ are depicted in Fig. 3.12. Assuming that the downconversion processes have equal probability amplitude, the state of the resonator at each frequency ξ is a superposition,

$$|\psi\rangle \quad = \quad \frac{1}{\sqrt{2}} \left(|1\rangle_{\tilde{a}_1} |1\rangle_{\tilde{a}_0} |0\rangle_{\tilde{a}_2} + |0\rangle_{\tilde{a}_1} |1\rangle_{\tilde{a}_0} |1\rangle_{\tilde{a}_2} \right). \tag{3.7}$$

First order process yields a tripartite state with bipartite squeezing correlations. Higher order multipartite state is present, but not studied. Our state (had the experiment been ideal) can be understood as a maximally entangled state between the mode $\tilde{a}_0$ and the bright state $\tilde{b}$. The bright state is a superposition of two modes $\tilde{a}_1$ and $\tilde{a}_2$. This does not contradict the monogamy [78] of entanglement.

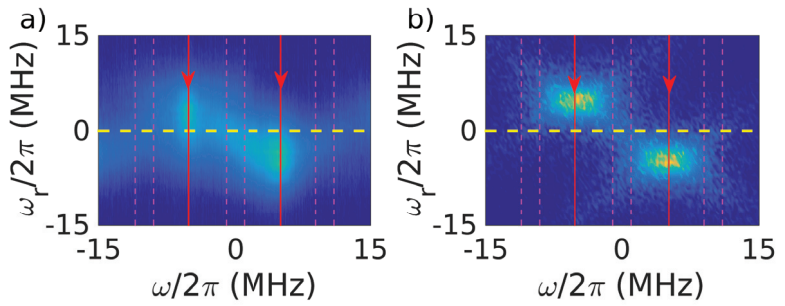

Figure 3.12. a) Observed noise power for fixed pump power and frequencies $\omega_1/4\pi = 4.995$ GHz, $\omega_2/4\pi = 5.005$ GHz at different values of the resonance frequency $\omega_{\mathrm{r}}/2\pi$ and measurement frequency $\omega/2\pi$ relative to $(\omega_1+\omega_2)/8\pi = 5$ GHz. The quality factor $\mathrm{Q} \approx 500$ with the pumps off. The dashed magenta lines along with the dashed yellow line indicate the measurement band and the bias point at which the correlation data were collected. The red lines indicate half of the pump frequencies. b) Numerically solved expectation based on Eq. 3.3. The inset depicts an exaggerated power spectrum on which the analyzed frequency bands are marked with dashed lines.

The "bright" and "dark" modes are introduced as follows:

$$\tilde{b}[\xi] \quad = \quad \cos\theta e^{-i\varphi_1} \tilde{a}[2\Delta_1 - \xi] + \sin\theta e^{-i\varphi_2} \tilde{a}[2\Delta_2 - \xi], \tag{3.8}$$

$$\tilde{d}[\xi] \quad = \quad \sin\theta e^{-i\varphi_1} \tilde{a}[2\Delta_1 - \xi] - \cos\theta e^{-i\varphi_2} \tilde{a}[2\Delta_2 - \xi]. \tag{3.9}$$

Here θ is a parameter to account for the asymmetry between the two pump powers, where φ_1 and φ_2 are the phase factors corresponding to the

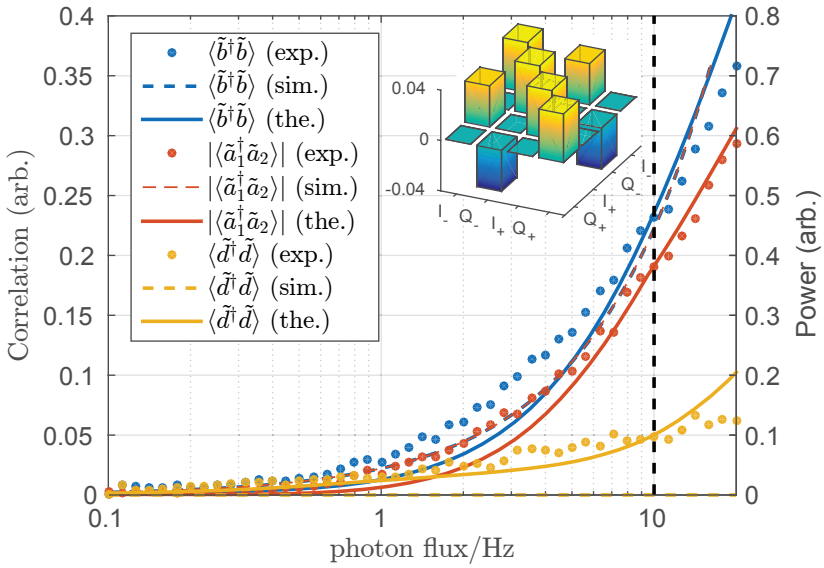

Figure 3.13. Measured correlators (specified in the inset label according notations of modes from Fig. 3.11) vs. photon flux/Hz from the cavity. The symbols refer to measured data, while the curves are predictions from theory (dashed) and simulations (solid). Our simulation reproduces also the residual population in the dark mode. The 3-D histogram represents the measured covariance matrix corresponding to the fields $\tilde{a}_0$ and $\tilde{a}_1$, where the two-mode quadratures are defined as $I_0 = \frac{a_0+a_0^\dagger}{2}$, $Q_0 = \frac{a_0-a_0^\dagger}{2i}$, $I_1 = \frac{a_1+a_1^\dagger}{2}$ and $Q_1 = \frac{a_1-a_1^\dagger}{2i}$, demonstrating two-mode squeezing correlations across the first pump.

individual pump phases. The significance of these is illustrated in Fig. 3.14a. The definition of the orthogonal bright and dark modes resembles a beamsplitter operation in frequency (rather than in space, as in usual interferometers). The simultaneous action of the two pumps results in coherence $\langle(\tilde{a}_{\rm out}[2\Delta_1-\xi])^\dagger\tilde{a}_{\rm out}[2\Delta_2-\xi']\rangle$ between the extremal frequencies $2\Delta_1-\xi$ and $2\Delta_2-\xi$, which is identified as vacuum induced coherence. The obtained measurement results along with theoretical predictions are depicted in Fig. 3.13.

An experiment was also conducted to study the effect when the two pumps were modulated by two mixers driven by two $1\mu s$ pulses with varying time offset. The full schematic for the measurement setup is depicted in Fig. 3.16. Theory predicts that as the pulse overlap is reduced, vacuum induced coherence will vanish while the squeezing correlations remain. Experimental results are depicted in Fig. 3.15.

In conclusion, we conducted detailed studies of coherence effects due to

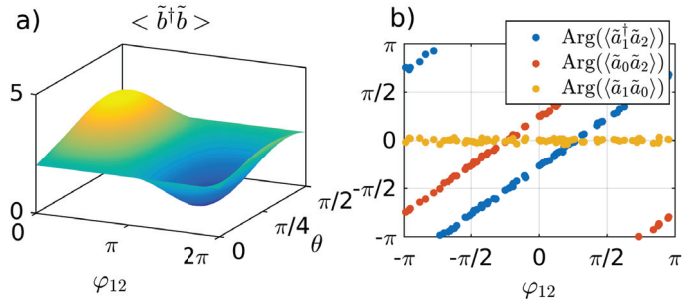

Figure 3.14. a) Bright/dark mode amplitude vs. relative observation phase $\varphi_{12} = \varphi_1 - \varphi_2$ and pump amplitude asymmetry θ. The maximum gives the bright mode amplitude and the minimum the dark mode. b) Angle of the correlations vs. φ_{12}.

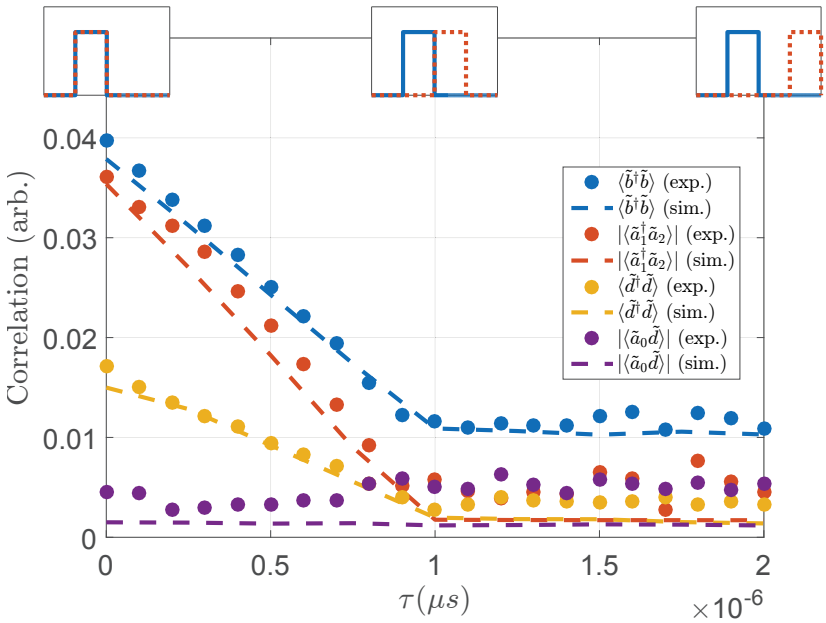

Figure 3.15. Vacuum induced coherence vs. the overlap time of pulsed pump tones. Correlation vanishes as the pulse overlap is reduced. The remaining correlation in $\langle \tilde{b}^\dagger \tilde{b} \rangle$ is due to slightly asymmetric pump power. This behaviour was reproduced by numerically solving Eq. 3.3.

vacuum fluctuations under double parametric pumping. A tripartite state with nonzero number of photons at three separate frequencies, squeezing correlations between neighboring frequency points and vacuum induced coherence between the extremal frequencies were observed and the observations were found to be in line with the theoretical predictions.

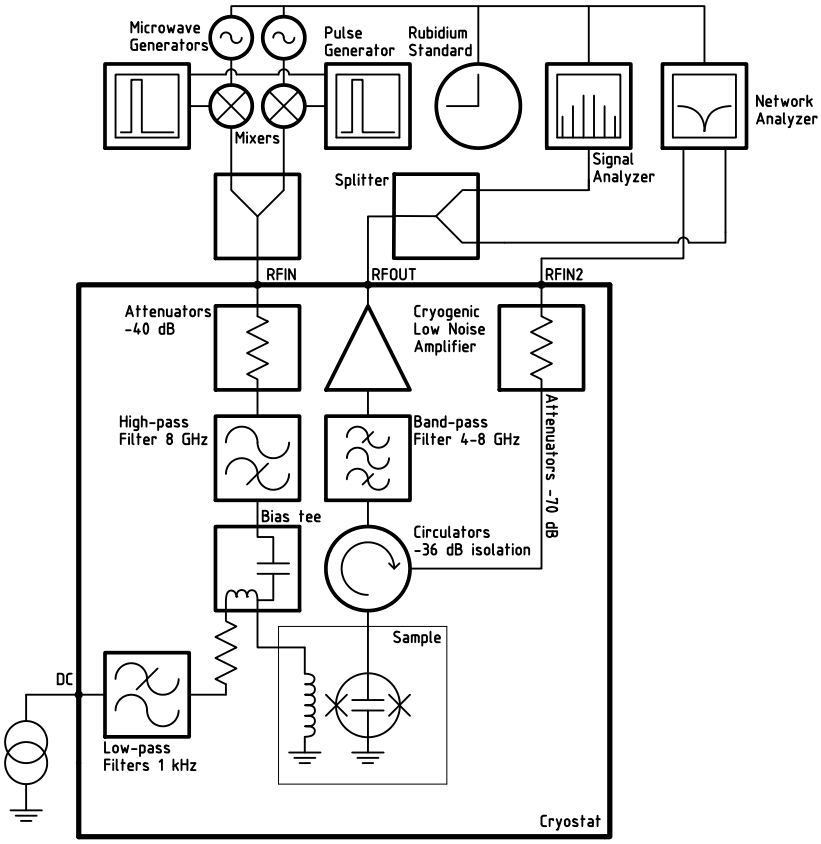

Figure 3.16. Schematic for the measurement setup including the pulse generators used to create the two overlapping 10 GHz pulses with tunable delay. All devices employed a common frequency reference derived from a rubidium atomic clock for improved phase stability.

4. Nanocarbon devices

This section gives an overview of Publication III and IV which both deal with experiments on nanocarbon devices, nanotubes and graphene. Publication III is discussed in Sect. 4.1 and Publication IV in Sect. 4.2.

4.1 Nanotube electrometer

In this work, a superconducting multiwalled carbon nanotube is used as a field-effect transistor (FET). The device is operated similarly to a regular RF-SET, but here the nanotube plays the role of the island and barriers are formed by the contact between the nanotube and the metallic reservoirs. The origin of superconductivity in the nanotube is via the proximity effect induced by superconducting Ti/Al leads [79–89].

The low impedance of the weak supercurrent branch of such a device is attractive because no impedance matching circuits are required to match the device to the characteristic 50Ω impedance. The device can instead be matched by tuning the gate charge, which modulates the critical current I_C, or by tuning the DC bias current. Carrier amplitude, through phase diffusion, affects the impedance level as well.

The device is operated as a wideband charge detector as follows. An electromagnetic wave injected from the room temperature travels along cold attenuators which eliminate high-temperature Johnson noise, the signal is reflected from the sample behind a bias tee. The reflection amplitude is sensitive to the impedance of the sample as described by Eq. 3.2. The reflection is modulated by the gate signal and, as a result, will mix some energy from the injected frequency to the sidebands similarly to amplitude modulation (AM).

The reflected wave is then of the form

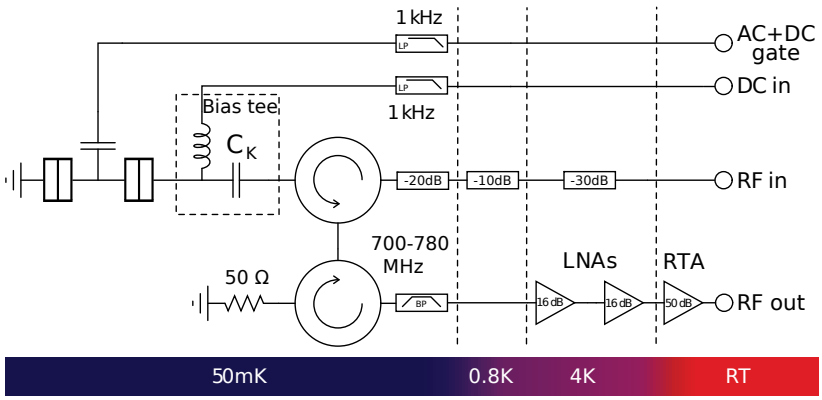

Figure 4.1. Schematic of the nanotube electrometer measurement with the sample marked as an SET.

$$V_{out}(t) = [\Gamma + \gamma_1 \cos(\Omega t)] V_{\rm in} \sin(\omega t) + \frac{\Gamma \gamma_1}{2} \left[\sin((\omega+\Omega)t) + \sin((\omega-\Omega)t)\right], \quad (4.1)$$

where Ω is the gate modulation frequency, and $V_{\rm in}$ the amplitude of the injected voltage at the sample and Γ_1 is the "reflection coefficient" of the sideband. For small δI_C, it is

$$\gamma_1 = -\frac{Z_0 Z^2}{(Z_0+Z)^2} \frac{\partial^2 I_{SD}}{\partial V_{SD} \partial I_C} \delta I_C. \quad (4.2)$$

Here $Z = (1/(-i\omega C_K) + 1/(-i\omega C + \partial I_{SD}/\partial V_{SD}))^{-1}$, with C_K as the coupling capacitance between the sample and the microwave measurement system.

The reflected carrier signal and the generated sidebands are directed by two circulators to low noise amplifiers whose input noise is prevented from flowing back to the sample by the circulators and their terminations. The output is read at the room temperature using a spectrum analyzer and charge sensitivity is deduced from the signal to noise ratio of the sidebands. The measurement scheme is depicted in Fig. 4.1.

Gate-voltage-induced charge modifies the critical current (see Fig. 4.2), which in turn changes the effective impedance of the junction under microwave irradiation. The device was probed for maximum sideband generation by sweeping the gate voltage V_G, bias I_{SD} and microwave pump power P_{MW}. The effective impedance of the sample can be tuned by changing all of these parameters to achieve a good impedance match without any extra matching elements. When operated well below the Joseph-

son frequency ($\omega \ll \omega_J$), it is the differential resistance R_d of the low-frequency IV-curve that governs the reflection.

The S/N was recorded at maximum sideband amplitude is depicted in Fig. 4.2b. By using a known AC-exitation on the gate as well as the gate capacitance C_G deduced from the period of the SET oscillations ($\Delta V_G = e/C_G = 130$ mV), a sensitivity of $3.1 \times 10^{-5} e/\sqrt{\text{Hz}}$ could be calculated.

In these measurements, a gate modulation frequency of 470 Hz was chosen. This frequency is far enough from the carrier not to suffer from the phase noise of the generator signal, but small enough not to suffer from frequency cutoffs due to filters in the employed DC lines.

The microwave signal in these measurements was in the 600-900 MHz range due to existing equipment. This frequency range is somewhat of a sweet spot in a sense that it is well above the flicker noise corner frequency, but low enough to have limited dissipation associated with the microwave components. Availability of passive circulators for isolation purposes is also an important benefit.

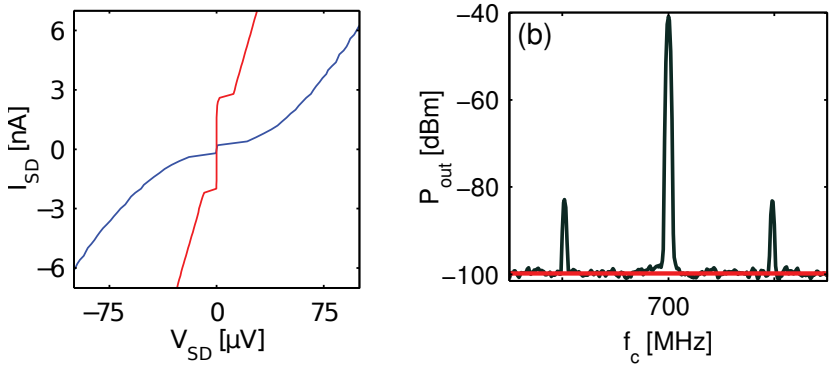

Figure 4.2. a) MWNT quantum dot IV-curves for two gate voltages giving maximum difference. b) Using a carrier power of -120 dBm, a charge sensitivity of $3.1 \times 10^{-5} e/\sqrt{\text{Hz}}$ was observed at $I_C = 1.3$ nA.

4.2 Cooper pair splitting in graphene

Splitting of a Cooper-pair (CPS) from a superconductor into two different normal metal terminals forms a pair of electrons with entangled spins [90,91]. Graphene is an ideal platform due to its large mean free path and weak spin-orbit coupling which promise long spin coherence times [92,93].

A double quantum dot (QD) system made of graphene with superconducting leads was measured. The QDs in our sample, contrary to other similar experiments so far, could be tuned independently. Based on conductance correlations and current splitting between separately biased output terminals while tuning over a resonance level, a splitting efficiency of 10% was obtained.

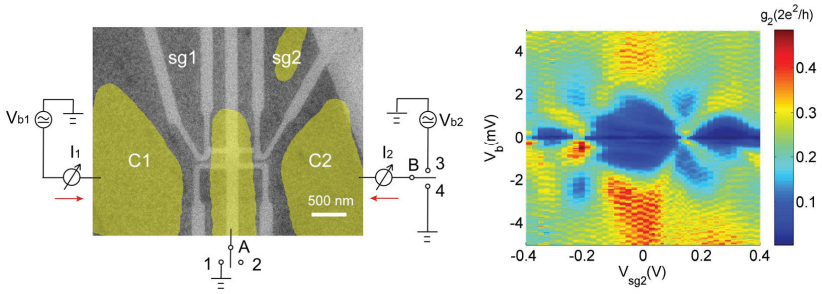

Figure 4.3. a) False color scanning electron micrograph of the graphene sample (graphene in dark grey). Ti/Al contacts are indicated in yellow. The light gray is the uncovered SiO_2 substrate. Two rectangle-shaped QDs and side-gates were done by EBL and oxygen plasma etching. b) Stability diagram of one of the QDs as a function of DC bias voltage and side gate voltage with back gate at $V = -14.49V$. The dark blue color in the low bias region indicates the superconducting gap. The addition energy varies over 1-4 meV while the width of the resonance peaks is 0.1-0.2 meV.

The sample was made by standard mechanical exfoliation of graphene and placed onto a highly doped silicon substrate coated with thermal SiO_2. The QDs were constructed with electron-beam lithography (EBL) techniques and by plasma etching through windows in a PMMA mask. Finally, another EBL step was done to deposit the superconducting contacts. The final device dimensions can be seen in Fig. 4.3a. Sample dimensions were chosen based on the coherence length, mean free path, and the goal of having small capacitive coupling between the QDs.

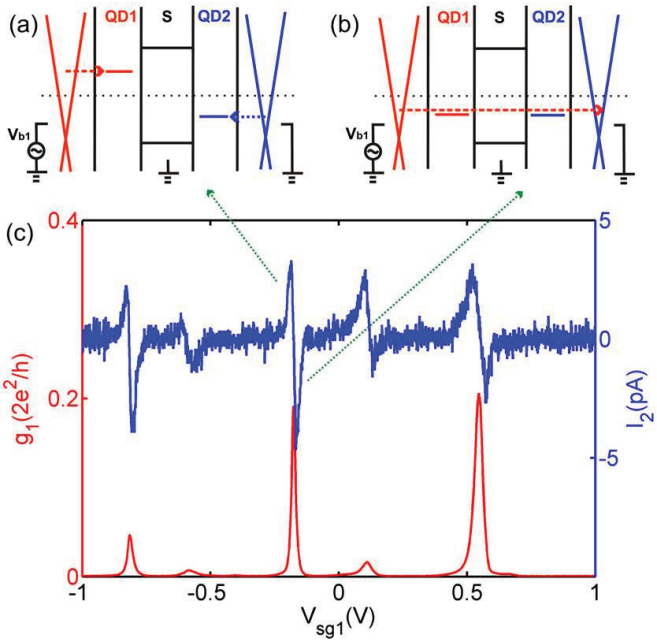

Figure 4.4. a) When the quantum dot energy levels are asymmetric, CPS dominates. b) Elastic cotunneling dominates if the levels are aligned. c) Conductance g_1 and nonlocal current I_2 as a function of sidegate voltage V_{sg1} at backgate voltage $V_{\mathrm{bg}} = 5V$ with AC bias on QD1 and the other terminals grounded.

The contribution of the CPS and EC are [95]

$$g_{CPS} = \frac{R_\square}{8} K_0 \left(\frac{\sqrt{2}r}{\xi} \right) \int \frac{g_1(E) g_2(-E)}{4T \cosh^2 E/2T} dE, \tag{4.3}$$

$$g_{EC} = \frac{R_\square}{8} K_0 \left(\frac{\sqrt{2}r}{\xi} \right) \int \frac{g_1(E) g_2(E)}{4T \cosh^2 E/2T} dE. \tag{4.4}$$

Here K_0 is the modified Bessel function, $g_1 = dI_1/dV_1$, $g_2 = dI_1/dV_2$ are the differential conductances of the quantum dots at $V_{1,2} = E/e$ and $R_\square$ the sheet resistance. Based on these equations, it is clear that while the energy levels of the two QDs are asymmetric, CPS is favoured. In the case of symmetric energy levels elastic cotunneling (EC) is preferred.

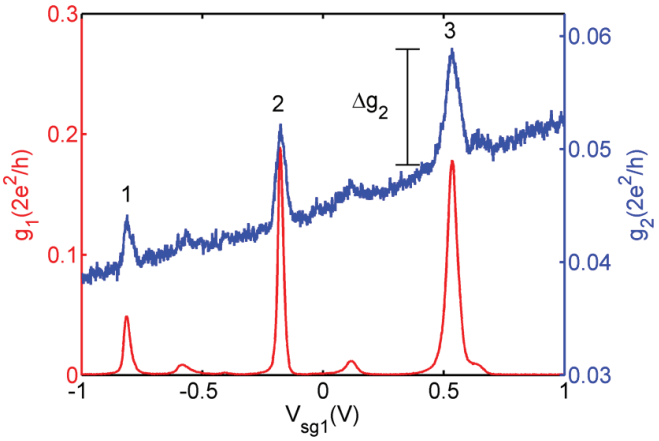

Figure 4.5. Differential conductance g_1 and g_2 of both QDs as a function of V_{sg1} with constant AC bias on both. When the energy level of QD1 crosses the Fermi level, electrons will tunnel easily through it. Because of high addition energy to QD1, transport of both electrons from a split Cooper pair will be suppressed and the other electron will instead more likely tunnel through QD2. As a result there is a corresponding peak in the conductance of the other QD as well. This nonlocal positive conductance correlation is regarded as evidence of CPS [94–118].

A maximum splitting efficiency of $\eta = 2\Delta g_2/(g_1 + g_2) = 0.1$ was observed in our conductance measurements. Here Δg_2 is the conductance increase in QD2 due to CPS. This value is two orders of magnitude higher than the theoretical estimate $\eta = 0.1\%$. This discrepancy is attributed to the influence of high Ohmic graphene ribbons which may lead to disorder-enhanced crossed Andreev reflection, as well as to the neglect of Coulomb interaction in the theory.

An alternate goal of this experiment was to study the entanglement of electrons directly by measuring the current-current cross correlation of radio-frequency noise emanating from the quantum dots. The principle for doing this is presented in Fig. 4.6. The current fluctuations from the sample will be recorded by two separate amplifier chains. Circulators are used to isolate the amplifier input noise and to prevent them from introducing unwanted cross-correlation through the sample. The signals are I/Q demodulated, digitized and further processed on a PC. A calibration sample can be connected via two microwave switches. This allows determination of the true power levels. Biasing circuitry and filters are not separately indicated in the schematic.

Additionally, we have acquired a PCI Express digitizer from Alazartech, (the ATS9440 for full 4 quadrature capture at 14-bit, 125 MS/s). Our system can process these data in nearly real time with over 90% duty cy-

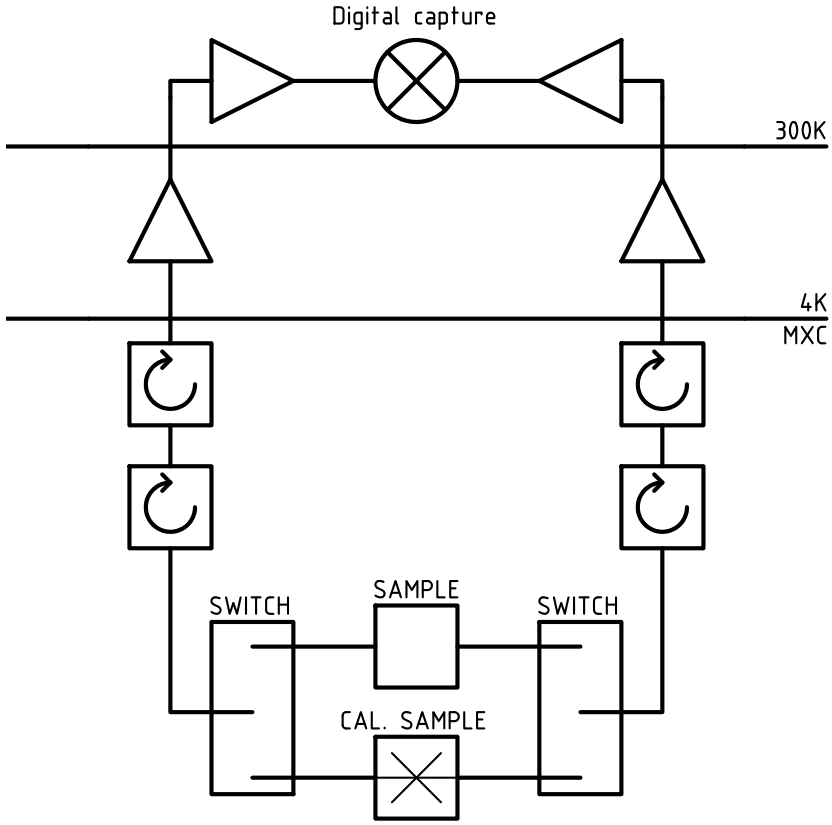

Figure 4.6. Setup to directly measure the entangled electron pairs by measuring the cross-correlation of the microwave noise from two sample terminals. Here, the mixer is simply a general correlator symbol, but in the actual setup it contains an I/Q demodulator and a digitizer, other mixing stages, additional amplifiers, etc.

cle. This is accomplished with the help of a fast graphics processing unit (GPU). The GPU is used for large-bandwidth parallel Fast Fourier Transforms that form an essential part of calculating the full cross-correlation functions. A large throughput is very useful in improving the speed and sensitivity of the measurement system and it compares extremely favourably, both in terms of performance and cost, to other methods such as direct capture of the waveforms by a fast oscilloscope. We have found that the use of GPU computation is less challanging and more flexible than application of FPGA technology; yet it offers comparable performance.

5. Conclusions and outlook

A range of superconducting nanodevices operated near the fundamental performance limits set by quantum mechanics have been studied in this thesis along with the nature of the quantum vacuum itself. These devices and techniques are among the most sensitive in the world: they shall undoubtedly be of interest to future generations of scientists and will perhaps even serve in the development of quantum information processing.

Besides being fundamental to the foundations of quantum mechanics, the study of quantum noise is also closely related to fundamental phenomena in the Universe such as Hawking radiation of black holes and evolution of the early Universe. Metamaterials based on Josephson junctions form a promising platform for studying such phenomena. Through black hole physics and quantum theory, there exists also a connection to holography and string theory [119]. Therefore, the present study of the quantum vacuum yields relevant insight of the possibilities how to adress the yet unknown aspects of fundamental physics.

Basic metamaterials research may offer several practical applications in the future. Recent years have brought great advances exemplified by negative index metamaterials, superlenses breaking the diffraction limit, invisibility cloaks and other devices utilizing the electromagnetic near-field etc.

Optimization of the cryogenic environment for all noise sources and extra dissipation is an extremely challenging and important task. This task is essential for experiments in need of the near quantum limited performance. None of the numerous samples tested in the experiments of this thesis appeared to be particularly good or optimal for what they were intended for. In fact, most of them were totally useless and extremely noisy, and only a few best of the best results were worth analyzing.

By far, the biggest challange is the quality of the standard photolitho-

graphic sample fabrication which was employed to provide the Nb-based microwave samples used in this thesis. There is an obvious need for significant improvements, in particular considering the realm of microwave experiments on junction arrays where unwanted inhomogeneity and dissipation cannot be tolerated. These improvements will become increasingly important should a need arise for wideband devices with even stricter quality requirements.

A brief study of some new and highly promising carbon nanomaterial devices was also conducted in this thesis. These devices, too, are so far plagued by poor manufacturing yield and lack of proper scalability. The fundamental physics behind them, however, appears to be rich and nanocarbon devices may yet offer unexpected paths to develop new technologies. There's also a small chance Moore's law may acquire a brief extention to its life span due to carbon nanotube electronics. The carbon nanotube and graphene work in this thesis, though, did not address traditional digital logic, but focused on fundamental research of mesoscopic physics.

Bibliography

[1] Josephson, B. D., Possible new effects in supercunductive tunneling, *Phys. Lett.*, **1**, 251-253 (1962).

[2] Likharev, K. K., *Dynamics of Josephson Junctions and Circuits*, Gordon and Breach, New York (1986).

[3] https://en.wikipedia.org/wiki/Superconducting_tunnel_junction

[4] Images by Santavicca, D. F.

[5] Heikkilä, T., *The Physics of Nanoelectronics*, Oxford University Press (2013).

[6] Tinkham, M., *Introduction to Superconductivity*, McGraw-Hill, New York (1996).

[7] Callen, H. B., Welton, T. A., Irreversibility and Generalized Noise, *Phys. Rev.*, **83**, 34 (1951).

[8] Mariantoni, M., Menzel, E. P., Deppe, F., Araque Caballero, M. Á., Baust, A., Niemczyk, T., Hoffmann, E., Solano, E., Marx, A., Gross, R., Planck Spectroscopy and Quantum Noise of Microwave Beam Splitters, *Phys. Rev. Lett.*, **105**, 133601 (2010).

[9] Leonhardt, U., *Measuring the Quantum State of Light*, Cambridge University Press (2005).

[10] Nation, P. D., Johansson, J. R., Blencowe, M. P., Nori, F., Colloquium: Stimulating uncertainty: Amplifying the quantum vacuum with superconducting circuits, *Rev. Mod. Phys.*, **84**, 1 (2012).

[11] Roch, N., Flurin, E., Nguyen, F., Morfin, P., Campagne-Ibarcq, P., Devoret, M. H., Huard, B., Widely tunable, non-degenerate three-wave mixing microwave device operating near the quantum limit, *Phys. Rev. Lett.*, **108**, 147701 (2012).

[12] Clerk, A. A., Devoret, M. H., Girvin, S. M., Marquardt F., Schoelkopf, R. J., Introduction to quantum noise, measurement, and amplification *Rev. Mod. Phys.*, **82**, 1155 (2010).

[13] Kraus, J. D., *Radio Astronomy*, McGraw-Hill (1966).

[14] Spietz, L., Schoelkopf, R. J., Pari, P., Shot noise thermometry down to 10 mK, *Appl. Phys. Lett.*, **89**, 183123 (2006).

[15] https://en.wikipedia.org/wiki/Spontaneous_parametric_down-conversion

[16] Hatridge, M., Vijay, R., Slichter, D. H., Clarke, J., Siddiqi, I., Dispersive magnetometry with a quantum limited SQUID parametric amplifier, *Phys. Rev. B.*, **83**, 134501 (2011).

[17] Yurke, B., Corruccini, L. R., Kaminsky, P. G., Rupp, L. W., Observation of parametric amplification and deamplification in a Josephson parametric amplifier, *Phys. Rev. A*, **39**, 2519–2533 (1989).

[18] Yurke, B., Roukes, M. L., Movshovich, R., Pargellis, A. N., A low-noise series-array Josephson junction parametric amplifier, *Appl. Phys. Lett.*, **69**, 3078–3080 (1996).

[19] Bergeal, N., Schackert, F., Metcalfe, M., Vijay, R., Manucharyan, V. E., Frunzio, L., Prober, D. E., Schoelkopf, R. J., Girvin, S. M., Devoret, M. H., Phase-preserving amplification near the quantum limit with a Josephson ring modulator, *Nature*, **465**, 64–68 (2010).

[20] Mück, M., Kycia, J. B., Clarke, J., Superconducting quantum interference device as a near-quantum-limited amplifier at 0.5 GHz, *Appl. Phys. Lett.*, **78**, 967–969 (2001).

[21] Asztalos, S. J., Carosi, G., Hagmann, C., Kinion, D., van Bibber, K., SQUID-based microwave cavity search for dark-matter axions, *Phys. Rev. Lett.*, **104**, 041301 (2010).

[22] Castellanos-Beltran, M. A., Irwin, K. D., Hilton, G. C., Vale, L. R., Lehnert, K. W., Amplification and squeezing of quantum noise with a tunable Josephson metamaterial, *Nature Physics*, **4**, 929–931 (2008).

[23] Teufel, J. D., Donner, T., Castellanos-Beltran, M. A., Harlow, J. W., Lehnert, K. W., Nanomechanical motion measured with precision beyond the standard quantum limit, *Nature Nanotech.*, **4**, 820–823 (2009).

[24] Castellanos-Beltran, M. A., Lehnert, K. W., A widely tunable parametric amplifier based on a SQUID array resonator, *Appl. Phys. Lett.*, **91**, 083509 (2007).

[25] Spietz, L., Irwin, K., Aumentado, K., Aumentado, J., Input impedance and gain of a gigaherz amplifier using a dc superconducting device in a quarter wave resonator, *Appl. Phys. Lett.*, **93**, 082506 (2008).

[26] Mears, C. A., Hu, Q., Richards, P. L., Worsham, A. H., Prober, D. E., Quantum-limited heterodyne detection of millimeter waves using superconducting tantalum tunnel junctions, *Appl. Phys. Lett.*, **57**, 2487–2489 (1990).

[27] Tiemann, J. J., Shot noise in tunnel diode amplifiers, *Proc. IRE.*, **8**, 1418–1423 (1960).

[28] Moore, G. T., Quantum theory of the electromagnetic field in a variable-length one-dimensional cavity, *J. Math. Phys.*, **11**, 2679–2691 (1970).

[29] Fulling, S. A., Davies, P. C. W., Radiation from a moving mirror in two dimensional space-time: Conformal anomaly, *Proc. R. Soc. Lond. A.*, **348**, 393–414 (1976).

[30] Yablonovitch, E., Accelerating reference frame for electromagnetic waves in a rapidly growing plasma: Unruh-Davies-Fulling-DeWitt radiation and the nonadiabatic Casimir effect, *Phys. Rev. Lett.*, **62**, 1742–1745 (1989).

[31] Schwinger, J., Casimir energy for dielectrics, *Proc. Natl. Acad. Sci. USA*, **89**, 4091–4093 (1993).

[32] Johansson, J. R., Johansson, G., Wilson, C. M., Nori, F., Dynamical Casimir effect in superconducting coplanar waveguide, *Phys. Rev. Lett.*, **103**, 147003–147006 (2009).

[33] Johansson, J. R., Johansson, G, Wilson, C. M., Nori, F., Dynamical Casimir effect in superconducting microwave circuits, *Phys. Rev. A*, **82**, 052509–052517 (2010).

[34] Fulling, S. A., *Aspects of Quantum Field Theory in Curved Space-Time*, Cambridge Univ. Press, Cambridge (1989).

[35] Crocce, M., Dalvit, D. A. R., Lombardo, F. C., Mazitelli, F. D., Model for resonant photon creation in a cavity with time-dependent conductivity, *Phys. Rev. A*, **70**, 033811-033816 (2004).

[36] Belgiorno, F., Cacciatori, S. L., Clerici, M., Gorini, V., Ortenzi, G., Rizzi, L., Rubino, E., Sala, V. G., Faccio, D., Hawking radiation from ultrashort laser pulse filaments, *Phys. Rev. Lett.*, **105**, 203901–203904 (2010).

[37] Wilson, C. M., Johansson, G., Pourkabirian, A., Simoen, M., Johansson, J. R., Duty, T., Nori, F., Delsing, P., Observation of the dynamical Casimir effect in a superconducting circuit, *Nature*, **479**, 376–379 (2011).

[38] Lambrecht, A., Jaekel, M.-T., Reynaud, S., Motion Induced Radiation from a Vibrating Cavity, *Phys. Rev. Lett.*, **77**, 615–618 (1996).

[39] Dodonov, V. V., Klimov, A. B., Generation and detection of photons in a cavity with a resonantly oscillating boundary, *Phys. Rev. A*, **53**, 2664–2682 (1996).

[40] Ji, J.-Y., Hyun-Hee, J., Park, J.-W., Soh, K.-S., Production of photons by the parametric resonance in the dynamical Casimir effect, *Phys. Rev. A*, **56**, 4440–4444 (1997).

[41] Schützhold, R., Plunien, G., Soff, G., Trembling cavities in the canonical approach, *Phys. Rev. A*, **57**, 2311–2318 (1998).

[42] Uhlmann, M., Plunien, G., Schützhold, R., Soff, G., Resonant cavity photon creation via the dynamical Casimir effect, *Phys. Rev. Lett.*, **93**, 193601–193604 (2004).

[43] Braggio, C., Bressi, G., Carugno, G., Del Noce, C., Galeazzi, G., Lombardi, A., Palmieri, A., Ruoso, G., Zanello, D., A novel experimental approach for the detection of the dynamical Casimir effect, *Europhys. Lett.*, **70**, 754–760 (2005).

[44] Kim, W.-J., Brownell, J. H., Onofrio, R. Detectability of dissipative motion in quantum vacuum via superradiance, *Phys. Rev. Lett.*, **96**, 200402–200405 (2006).

[45] De Liberato, S., Gerace, D., Carusotto, I., Ciuti, C., Extracavity quantum vacuum radiation from a single qubit, *Phys. Rev. A*, **80**, 053810 (2009).

[46] Dodonov, V. V., Current status of the Dynamical Casimir effect, *Phys. Scripta*, **82**, 038105–038114 (2010).

[47] Walls, D. F., Milburn, G. J., *Quantum Optics*, Springer, Secaucus NJ (2008).

[48] Eichler, C., Bozyigit, D., Lang, C., Baur, M., Steffen, L., Fink, J. M., Filipp, S., Wallraff, A., Observation of two-mode squeezing in the microwave frequency domain, *Phys. Rev. Lett.*, **107**, 113601–113604 (2011).

[49] Caves, C. M., Schumaker, B. L., New formalism for two-photon quantum optics. I. Quadrature phases and squeezed states, *Phys. Rev. A*, **31**, 3068–3092 (1985).

[50] Simon, R., Peres-Horodecki separability criterion for continuous variable systems, *Phys. Rev. Lett.*, **84**, 2726–2729 (2000).

[51] Giedke, G., Wolf, M., Krüger, O., Werner, R., Cirac, J., Entanglement of formation for symmetric Gaussian states, *Phys. Rev. Lett.*, **91**, 107901 (2003).

[52] Ou, Z. Y., Pereira, S. F., Kimble, H. J., Peng, K. C., Realization of the Einstein-Podolsky-Rosen paradox for continuous variables, *Phys. Rev. Lett.*, **68**, 3663–3666 (1992).

[53] Braunstein, S. L., van Loock, P. Quantum information with continuous variables, *Rev. Mod. Phys.*, **77**, 513–575 (2005).

[54] You, J. Q., Nori, F., Atomic physics and quantum optics using superconducting circuits, *Nature*, **474**, 589-597 (2011).

[55] Yurke, B., Kaminsky, P. G., Miller, R. E., Whittaker, E. A., Smith, A. D., Silver, A. H., Simon, R. W., Observation of 4.2-K equilibrium-noise squeezing via a Josephson-parametric amplifier, *Phys. Rev. Lett.*, **60**, 764-767 (1988).

Nat. Phys., **4**, 929–931 (2008).

[56] Mallet, F., Castellanos-Beltran, M. A., Ku, H. S, Glancy, S., Knill, E., Irwin, K. D., Hilton, G. C., Vale, L. R., Lehnert, K. W., Quantum State Tomography of an Itinerant Squeezed Microwave Field, *Phys. Rev. Lett.*, **106**, 220502 (2011).

[57] Menzel, E. P., Di Candia, R., Deppe, F., Eder, P., Zhong, L., Ihmig, M., Haeberlein, M., Baust, A., Hoffmann, E., Ballester, D., Inomata, K., Yamamoto, T., Nakamura, Y., Solano, E., Marx, A., Gross, R., Path Entanglement of Continuous-Variable Quantum Microwaves, *Phys. Rev. Lett.*, **109**, 250502 (2012).

[58] Braunstein, S. L., van Loock, P., Quantum information with continuous variables, *Rev. Mod. Phys.*, **77**, 513–577 (2005).

[59] Zou, X. Y., Wang, L. J., Mandel, L., Induced coherence and indistinguishability in optical interference, *Phys. Rev. Lett.*, **67**, 318–321 (1991).

[60] Kim, Y.-H., Yu, R., Kulik, S. P., Shih, Y., Scully, M. O., Delayed "Choice" Quantum Eraser, *Phys. Rev. Lett.*, **84**, 1-5 (2000).

[61] Yuen, H. P., Two-photon coherent states of the radiation field, *Phys. Rev. A*, **13**, 2226-2243 (1976).

[62] Kelly, W. R., Dutton, Z., Schlafer, J., Mookerji, B., Ohki, T. A., Kline, J. S., Pappas, D. P., Direct observation of coherent population trapping in a superconducting artificial atom, **Phys. Rev. Lett.**, **104**, 1-4 (2010).

[63] Marquardt, F., Chen, J. P., Clerk, A. A., Girvin, S. M., Quantum Theory of Cavity-Assisted Sideband Cooling of Mechanical Motion, *Phys. Rev. Lett.*, **99**, 093902 (2007).

[64] Zakka-Bajjani, Nguyen, F., Lee, M., Vale, L. R., Simmonds, R. W., Aumentado, J., Quantum superposition of a single microwave photon in two different 'colour' states, *Nat. Phys.*, **7**, 599-603 (2011).

[65] Kiviranta, M., Brandel, O., Grönberg, L., Kunert, J., Linzen, S., Beev, N., Prunnila, M., Multilayer fabrication process for josephson junction circuits cross-compatible over two foundries, *Supercond. Sci. Technol.*, **submitted** (2015).

[66] Arimondo, E., Wolf, E., Coherent population trapping in laser spectroscopy, *Prog. Opt.*, **35**, 257-354 (1996).

[67] Tanji-Suzuki, H., Chen, W., Landig, R., Simon, J., Vuletic, V., Vacuum-Induced Transparency, **Science**, **333**, 1266-1269 (2011).

[68] Agarwal, G. S., *Quantum Optics*, Cambridge University Press (2012).

[69] Zhu, X., Matsuzaki, Y., Amsüss, R., Kakuyanagi, K., Shimo-Oka, T., Mizuochi, N., Nemoto, K., Semba, K., Munro, W. J., Saito, S., Observation of dark states in a superconductor diamond quantum hybrid system, *Nat. Commun.*, **5**, 3424 (2014).

[70] Kumar, K. S., Vepsalainen, A., Danilin, S., Paraoanu, G. S., Stimulated Raman adiabatic passage in a three-level superconducting circuit, arXiv 1508.02981v1 (2015).

[71] Ramelow, S., Ratschbacher, L., Fedrizzi, A., Langford, N. K., Zeilinger, A., Discrete tunable color entanglement, *Phys. Rev. Lett.*, **103**, 2-5 (2009).

[72] Lemos, G. B., Borish, V., Cole, G. D., Ramelow, S., Lapkiewicz, R., Zeilinger, A., Quantum imaging with undetected photons, *Nature*, **512**, 409-412 (2014).

[73] Ma, X.-S., Kofler, J., Zeilinger, A., Delayed-choice gedanken experiments and their realizations, arXiv:1407, (2014).

[74] Bertet, P., Osnaghi, S., Rauschenbeutel, A., Nogues, G., Auffeves, A., Brune, M., Raimond, J. M, Haroche, S., A complementarity experiment with an interferometer at the quantum-classical boundary, *Nature*, **411**, 166-170 (2001).

[75] da Silva, M. P., Bozyigit, D., Wallraff, A., Blais, A., Schemes for the observation of photon correlation functions in circuit QED with linear detectors, *Phys. Rev. A*, **82**, 043804 (2010).

[76] Chen, M., Menicucci, N. C., Pfister, O., Experimental Realization of Multipartite Entanglement of 60 Modes of a Quantum Optical Frequency Comb, *Phys. Rev. Lett.*, **112**, 120505 (2014).

[77] Bruschi, D., Sabín, C., Kok, P., Towards universal quantum computation through relativistic motion, arXiv 1311.5619v2 (2013).

[78] Terhal, B. M., Is Entanglement Monogamous?, *IBM J. Res. Dev.*, **48**, 71 (2004).

[79] Kasumov, A. Y., Deblock, R., Kociak, M., Reulet, B., Bouchiat, H., Khodos, I. I., Gorbatov, Y. B., Volkov, V. T., Journet, C., Burghard, M., Supercurrents through single-walled carbon nanotubes, *Science*, **284**, 1508 (1999).

[80] Morpurgo, J., Kong, A. F., Marcus, C. M., Dai, H., Gate-Controlled Superconducting Proximity Effect in Carbon Nanotubes, *Science*, **286**, 263 (1999).

[81] Kasumov, A., Kociak, M., Ferrier, M., Deblock, R., Guéron, S., Reulet, B., Khodos, I., Stéphan, O., Bouchiat, H., Quantum transport through carbon nanotubes: Proximity-induced and intrinsic superconductivity, *Phys. Rev. B*, **68**, 214521 (2003).

[82] Jarillo-Herrero, P., van Dam, J. A., Kouwenhoven, L. P., Quantum supercurrent transistors in carbon nanotubes, *Nature*, **439**, 953 (2006).

[83] Jorgensen, H. I. J., Grove-Rasmussen, K., Novotný, T., Flensberg, K., Lindelof, P. E., Electron Transport in Single-Wall Carbon Nanotube Weak Links in the Fabry-Perot Regime, *Phys. Rev. Lett.*, **96**, 207003 (2006).

[84] Cleuziou, J., Wernsdorfer, W., Bouchiat, V., Ondaruhu, T., Monthioux, M., Carbon nanotube superconducting quantum interference device, *Nat. Nanotechnol.*, **1**, 53 (2006).

[85] Wu, F., Danneau, R., Queio, P., Kauppinen, E., Tsuneta, T., Hakonen, P., Single-walled carbon nanotube weak links in Kondo regime with zero-field splitting, *Phys. Rev. B*, **79**, 073404 (2009).

[86] Vecino, E., Buitelaar, M., Martin-Rodero, A., Schönenberger, C., Levy Yeyati, A., Conductance properties of nanotubes coupled to superconducting leads: signatures of Andreev states dynamics, *Solid State Commun.*, **131**, 625 (2004).

[87] Haruyama, J., Tokita, A., Kobayashi, N., Nomura, M., Miyadai, S., Takazawa, K., Takeda, A., Kanda, Y., End-bonding multiwalled carbon nanotubes in alumina templates: Superconducting proximity effect, *Appl. Phys. Lett.*, **84**, 4714 (2004).

[88] Takesue, I., Haruyama, J., Kobayashi, N., Chiashi, S., Maruyama, S., Sugai, T., Shinohara, H., Superconductivity in Entirely End-Bonded Multiwalled Carbon Nanotubes, *Phys. Rev. Lett.*, **96**, 057001 (2006).

[89] Tsuneta, T., Lechner, L., Hakonen, P. J., Gate-Controlled Superconductivity in a Diffusive MultiwalledCarbon Nanotube, *Phys. Rev. Lett.*, **98**, 087002 (2007).

[90] Lesovik, G. B., Martin, T., Blatter, G., Electronic entanglement in the vicinity of a superconductor, *Eur. Phys. J. B*, **24**, 287 (2001).

[91] Recher, P., Sukhorukov, E. V., Loss, D., Andreev-tunneling, Coulomb blockade, and resonant transport of non-local spin-entangled electrons, *Phys. Rev. B*, **63**, 165314 (2001).

[92] Loss, D., DiVincenzo, D. P., Quantum computation with quantum dots, *Phys. Rev. A*, **57**, 120 (1998).

[93] Beckmann, D., Weber, H. B., v. Löhneysen, H., Evidence for Crossed Andreev Reflection in Superconductor-Ferromagnet Hybrid Structures, *Phys. Rev. Lett.*, **93**, 197003 (2004).

[94] Russo, S., Kroug, M., Klapwijk, T. M., Morpurgo, A. F., Experimental Observation of Bias-Dependent Nonlocal Andreev Reflection, *Phys. Rev. Lett.*, **95**, 027002 (2005).

[95] Cadden-Zimansky, P., Wei, J., Chandrasekhar, V., Cooper-pair-mediated coherence between two normal metals, *Nat. Phys.*, **5**, 393 (2009).

[96] Wei, J., Chandrasekhar, V., Positive noise cross-correlation in hybrid superconducting and normal-metal three-terminal devices, *Nat. Phys.*, **6**, 494 (2010).

[97] Hofstetter, L., Csonka, S., Nygård, J., Schönenberger, C., Cooper pair splitter realized in a two-quantum-dot Y-junction, *Nature*, **461**, 960 (2009).

[98] Hofstetter, L., Csonka, S., Baumgartner, A., Fulop, G., d'Hollosy, S., Nygård, J., Schönenberger, C., Finite-Bias Cooper Pair Splitting, *Phys. Rev. Lett.*, **107**, 136801 (2011).

[99] Das, A., Ronen, Y., Heiblum, M., Mahalu, D., Kretinin, A. V., Shtrikman, H., Correlated spin currents generated by resonant-crossed Andreev reflections in topological superconductors, *Nat. Commun.*, **3**, 1165 (2012).

[100] Herrmann, L. G., Portier, F., Roche, P., Yeyati, A. L., Kontos, T., Strunk, C., Carbon Nanotubes as Cooper-Pair Beam Splitters, *Phys. Rev. Lett.*, **104**, 026801 (2010).

[101] Schindele, J., Baumgartner, A., Schönenberger, C., Near-Unity Cooper Pair Splitting Efficiency, *Phys. Rev. Lett.*, **109**, 157002 (2012).

[102] Cayssol, J., Crossed Andreev Reflection in a Graphene Bipolar Transistor, *Phys. Rev. Lett.*, **100**, 147001 (2008).

[103] Benjamin, C., Pachos, J. K., Detecting entangled states in graphene via crossed Andreev reflection, *Phys. Rev. B*, **78**, 235403 (2008).

[104] Black-Schaffer, A. M., Edge Properties and Majorana Fermions in the Proposed Chiral d-Wave Superconducting State of Doped Graphene, *Phys. Rev. Lett.*, **109**, 197001 (2012).

[105] Chamon, C., Hou, C. Y., Mudry, C., Ryu, S., Santos, L., Masses and Majorana fermions in graphene, *Phys. Scripta*, **T146**, 014013 (2012).

[106] Heersche, H. B., Jarillo-Herrero, P., Oostinga, J. B., Vandersypen, L. M. K., Morpurgo, A. F., Bipolar Supercurrent in Graphene, *Nature*, **446**, 56 (2007).

[107] Dirks, T., Hughes, T. L., Lal, S., Uchoa, B., Chen, Y. F., Chialvo, C., Goldbart, P. M., Mason, N., Transport through Andreev bound states in a graphene quantum dot, *Nat. Phys.*, **7**, 386 (2011).

[108] Guttinger, J., Molitor, F., Stampfer, C., Schnez, S., Jacobsen, A., Droscher, S., Ihn, T., Ensslin, K., Transport through graphene quantum dots, *Rep. Prog. Phys.*, **75**, 126502 (2012).

[109] Feinberg, D., Andreev scattering and cotunneling between two superconductor-normal metal interfaces: the dirty limit, *Eur. Phys. J. B*, **36**, 419 (2003).

[110] Golubev, D. S., Kalenkov, M. S., Zaikin, A. D., Crossed Andreev Reflection and Charge Imbalance in Diffusive Normal-Superconducting-Normal Structures, *Phys. Rev. Lett.*, **103**, 067006 (2009).

[111] Dorokhov, O. N., On the coexistence of localized and extended electronic states in the metallic phase, *Solid State Commun.*, **51**, 381 (1984).

[112] Lesovik, G. B., Sadovskyy, I. A., Scattering matrix approach to the description of quantum electron transport, *Phys. Usp.*, **54**, 1007 (2011).

[113] Leijnse, M., Flensberg, K., Coupling Spin Qubits via Superconductors, *Phys. Rev. Lett.*, **111**, 060501 (2013).

[114] Sadovskyy, I. A., Lesovik, G. B., Vinokur, V. M., Unitary limit in crossed Andreev transport, arXiv:1412.8145 (2014).

[115] Chevallier, D., Rech, J., Jonckheere, T., Martin, T., Current and noise correlations in a double-dot Cooper-pair beam splitter, *Phys. Rev. B*, **83**, 125421 (2011).

[116] van der Wiel, W. G., De Franceschi, S., Elzerman, J. M., Fujisawa, T., Tarucha, S., Kouwenhoven, L. P., Electron transport through double quantum dots, *Rev. Mod. Phys.*, **75**, 1 (2003).

[117] Tan, Z. B., Puska, A., Nieminen, T., Duerr, F., Gould, C., Molenkamp, L. W., Trauzettel, B., Hakonen, P. J., Shot noise in lithographically patterned graphene nanoribbons, *Phys. Rev. B*, **88**, 245415 (2013).

[118] Libisch, F., Stampfer, C., Burgdörfer, J., Graphene quantum dots: Beyond a Dirac billard, *Phys. Rev. B*, **79**, 115423 (2009).

[119] Li, H., Li, L., Wang, Y., Zhang, H., Non-relativistic Josephson junction from holography, *J. High Energy Phys.*, **12**, 099 (2014).

"I am enough of an artist to draw freely upon my imagination. Imagination is more important than knowledge. Knowledge is limited. Imagination encircles the world." -- A. Einstein

Aalto-DD 13/2016

ISBN 978-952-60-6627-1 (printed)
ISBN 978-952-60-6628-8 (pdf)
ISSN-L 1799-4934
ISSN 1799-4934 (printed)
ISSN 1799-4942 (pdf)

Aalto University
School of Science
Low Temperature Laboratory, Department of Applied Physics
www.aalto.fi